

Contents lists available at ScienceDirect

Petroleum Science

journal homepage: www.keaipublishing.com/en/journals/petroleum-science



Original Paper

Numerical analysis of dispersion, attenuation, and seismic effects in a porous rock saturated with three-phase immiscible fluids



Xin Luo ^{a, b, *}, Xue-Hua Chen ^{a, b}, Tong Li ^b, Gui-Rong Luo ^c, Peng Wang ^d

- a State Key Laboratory of Oil & Gas Reservoir Geology and Exploitation, Chengdu University of Technology, Chengdu, 610059, Sichuan, China
- ^b College of Geophysics, Chengdu University of Technology, Chengdu, 610059, Sichuan, China
- ^c Oianan Oil Production Plant, Songyuan, Petrochina Iilin Oilfield Branch Company, Songyuan, 138000, Iilin, China
- ^d CCTEG Coal Mining Research Institute, Beijing, 100013, China

ARTICLE INFO

Article history: Received 26 September 2024 Received in revised form 9 February 2025 Accepted 24 April 2025 Available online 26 April 2025

Edited by Meng-Jiao Zhou

Keywords:
Multiphase immiscible fluids
Dispersion
Attenuation
Relative permeability
Capillary parameter
Seismic responses

ABSTRACT

Multiphase flow in porous rock is of great importance in the application of many industrial processes, including reservoir delineation, enhanced oil recovery, and CO2 sequestration. However, previous research typically investigated the dispersive behaviors when rock saturated with single or two-phase fluids and conducted limited studies on three-phase immiscible fluids. This study investigated the seismic dispersion, attenuation, and reflection features of seismic waves in three-phase immiscible fluidsaturated porous rocks. First, we proposed the calculation formulas of effective fluid modulus and effective fluid viscosity of multiphase immiscible fluids by taking into account the capillary pressure, reservoir wettability, and relative permeability simultaneously. Then, we analysed the frequencydependent behaviors of three-phase immiscible fluid-saturated porous rock under different fluid proportion cases using the Chapman multi-scale model. Next, the seismic responses are analysed using a four-layer model. The results indicate that the relative permeability, capillary pressure parameter, and fluid proportions are all significantly affect dispersion and attenuation. Comparative analyses demonstrate that dispersion and attenuation can be observed within the frequency range of seismic exploration for a lower capillary parameter α_3 and higher oil content. Seismic responses reveal that the reflection features, such as travel time, seismic amplitude, and waveform of the bottom reflections of saturated rock and their underlying reflections are significantly dependent on fluid proportions and capillary parameters. For validation, the numerical results are further verified using the log data and real seismic data. This numerical analysis helps to further understand the wave propagation characteristics for a porous rock saturated with multiphase immiscible fluids.

© 2025 The Authors. Publishing services by Elsevier B.V. on behalf of KeAi Communications Co. Ltd. This is an open access article under the CC BY license (http://creativecommons.org/licenses/by/4.0/).

1. Introduction

Velocity dispersion and energy attenuation caused by wave-induced fluid flow (WIFF) when seismic waves travel through the fluid-bearing porous media are important parameters for delineating hydrocarbon reservoirs (Pride et al., 2004; Batzle et al., 2006; Quintal, 2012; Luo et al., 2023; Guo et al., 2022, 2023; Zhao et al., 2023). It is generally agreed that the phenomenon of WIFF associated with wave energy loss results from the local and/or global pressure gradients (Biot, 1956a, 1956b; Brajanovski et al., 2005; Caspari et al., 2014; Dvorkin et al., 1994; He et al., 2021; Masson

et al., 2006; Müller et al., 2010; Quintal et al., 2019) and the frequency band in which dispersion and attenuation occur is closely related to the internal structure of the rock and fluid type (Chapman et al., 2003; Carcione and Picotti, 2006; Rubino et al., 2012; Chen et al., 2016a; Wang et al., 2017). Besides, for porous rock saturated with multiphase fluids, the dispersive behaviors are also dependent on the saturation, relative permeability, fluid proportion, capillary pressure parameter, wettability, and so on (Qi et al., 2014; Chen et al., 2017; Papageorgiou and Chapman, 2017; Li et al., 2022; Luo et al., 2022). Meanwhile, the dispersion and attenuation caused by the WIFF also influenced by factors such as pressure, stress and thermal fields (Chen et al., 2022, 2023). Therefore, taking into account the effects of various factors can assist in better understanding the WIFF mechanism that induces

E-mail address: luoxinfd90@163.com (X. Luo).

^{*} Corresponding author.

dispersion and attenuation in a porous media containing multiphase immiscible fluids.

Over the past few decades, the Biot Theory (Biot, 1956a, 1956b) has been widely used to explore the global flow attenuation mechanism of the macroscale whereas it ignores the impact of microscopic pore structure on velocity dispersion and attenuation of the seismic waves in propagation (Mochizuki, 1982; Dvorkin et al., 1995; Arntsen and Carcione, 2001). Besides, this theory is applicable to study the dispersive effects in the ultrasonic frequency band when rock is high permeability and uniformly saturated under the case of high pressure (King and Marsden, 2002; Mavko et al., 2009). Mavko and Nur (1975) proposed a squirt flow model which believes that the local flow of pore fluid is a key cause of the dispersion and attenuation, and provided a reasonable explanation for the strong attenuation of seismic waves. Further, a Biot-Squirt (BISQ) model was developed by combining the Biot theory and squirt flow theory (Dvorkin and Nur, 1993), which considers the effects of global and local flow on dispersion and attenuation while being incompatible with Gassmann theory at low frequencies. Chapman et al. (2002) proposed a new elastic model according to the squirt flow theory. This model indicates that the dispersion and attenuation induced by the fluid flow can both happen in the fracture scale and grain scale and can delineate frequency-dependent anisotropy of fluid-bearing fractured porous rock. Subsequently, more studies indicate that the squirt flow is a vital mechanism of dispersion and attenuation and it is mainly caused by the pressure gradient on the interface between fluids and the background (Chapman et al., 2003; Brajanovski et al., 2005; Jakobsen and Chapman, 2009; Gurevich et al., 2010). Recently, the dispersion and attenuation over a wider frequency range are of great interest in theoretical and experimental studies and with a very active research community (Batzle et al., 2006; de Paula et al., 2012; Zhao et al., 2013; Borgomano et al., 2019; Alkhimenkov et al., 2020; Sun and Gurevich, 2020; Gallagher et al., 2022; He et al., 2024; Chen et al., 2025). However, these models and theories are more suited to characterizing the impact of WIFF when a porous rock saturates a single fluid, as opposed to real rocks saturated with multiple fluids.

Subsequent works on the theory of porous media with twophase fluids are developed while differing in the details of implementation. White (1975) first described the state of fluid distribution using a patchy saturation model which can explain the mechanism of dispersion and attenuation for porous rock containing two-phase fluids. Subsequently, this model is further extended by many researchers to explore the seismic attenuation of a partially saturated rock (Dutta and Ode, 1979a, 1979b; Johson, 2001; Pride et al., 2004; Rubino et al., 2012) and indicates that the WIFF of a viscous fluid on the mesoscopic scale is a major cause of velocity dispersion and attenuation in a frequency range of seismic exploration. The past decade has seen an increase in the study of dispersion and attenuation mechanisms in partially saturated rocks (Tisato and Quintal, 2013; Dupuy and Stovas, 2014; Kuteynikova et al., 2014; Zhang and He, 2015; Jin et al., 2018; Qin et al., 2018; Ma et al., 2021). Recently, Liao et al. (2023) proposed a viscoelastic Chapman model to analyse the frequency-dependent anisotropy in partially saturated rocks containing two-phase immiscible fluids. Many researches demonstrate that, for a partially saturated porous rock, the saturation levels and fluid type have a substantial impact on the dispersion and attenuation (Chen et al., 2016a, 2017; Zhang et al., 2018; Li et al., 2020). Furthermore, the capillary parameter and relative permeability are also critical factors controlling the WIFF in porous rocks and directly affect the contribution of the dispersion and attenuation. Thus, the influence of capillarity effect on the dispersion and attenuation for patchysaturated rocks are investigated (Qi et al., 2014). Then, a model considering the effects of capillary pressure is proposed to explore the squirt flow impacts of a porous medium saturated with twophase fluids (Papageorgiou and Chapman, 2015). Further, a new rock-physis model that contains a parameter associated with capillary pressure is developed to illustrate the capillary behaviors at the microscopic scale for a rock saturated with two-phase immiscible fluids (Papageorgiou et al., 2016). Building on the previous work, Papageorgiou and Chapman (2017) studied the propagation characteristics of seismic waves in a porous medium saturated by two-phase immiscible fluids using a static capillary pressure parameter and a relative permeability model, indicating that the dispersive effects in the range of seismic frequency band are both depended on capillary pressure parameter and relative permeability. Besides, the frequency-dependent anisotropy is further analysed (Jin et al., 2018) according to the studies proposed by Papageorgiou and Chapman (2017), concluding that the mechanisms of the squirt and patch are both important for seismic wave propagation. However, the relative permeability model used in the abovementioned studies is only associated with saturation, ignoring the influence of the wettability on the relative permeability curves. It is widely accepted that rock wettability significantly affects the spatial distribution of fluids (Zhao et al., 2016; Zhao and Mohanty, 2019; Li et al., 2020). Wettability's influence on multiphase fluids flow in porous rock continues to challenge the descriptions in microscopic and macroscopic scales. Ignoring the effect of wettability on wave propagation may result in inaccuracies and misunderstanding of experimental and field test results. Therefore, numerical analysis and laboratory experiments are conducted to investigate the features of velocity dispersion and energy attenuation in porous medium when the factors of wettability, relative permeability and capillary parameter are considered (Li et al., 2022; Luo et al., 2022). However, previous research has focused on studying the wave characteristics during seismic wave propagation through the rock saturated with single or two-phase fluids. There has been limited studies on the behavior of dispersion and attenuation when a porous rock saturated with threephase immiscible fluids.

Multiphase flow in porous rock is of great importance in the application of many industrial processes, including reservoir delineation, enhanced oil recovery, and geologic CO_2 sequestration. Three immiscible fluids distributed in a porous medium is a common phenomenon and it occurs in a variety of natural and industrial processes. The question arises what happens to properties of seismic wave as they travel through a rock saturated with threephase immiscible fluids with different saturations? However, it's hard to observe the contributions of these multiple factors to the dispersion and attenuation when a rock saturated with three-phase immiscible fluids in some laboratory experiments and real seismic data. Therefore, numerical modeling is potentially important. Chen et al. (2016b, 2017) numerically analysed the frequency-dependent attenuation, velocity dispersion, and seismic effects in a porous rock saturated with three-phase fluids by employing Chapman's theory. However, the studies assume that the multiphase fluids are uniformly mixed and only consider the impact of the mixed fluid viscosity on dispersion and attenuation. Ahmad et al. (2020) also analysed the features of dispersion and attenuation of a porous medium containing three coexisting fluid phases and demonstrated that saturation significantly affects the characteristics of the seismic wave. However, previous studies do not provide sufficient evidence about the effects of capillary pressure parameter, relative permeability, and rock wettability on the behaviors of the dispersion and attenuation for three-phase immiscible fluids saturated porous rock.

In this paper, a relative permeability model that depends on the saturation, fluid viscosity and wettability is used to delineate the

fluid flow features of a porous medium containing three-phase immiscible fluids. In the numerical studies, we investigated the velocity dispersion and attenuation of a porous rock saturated with three-phase immiscible fluids and analysed the seismic effects. First, we proposed the calculation formulas of effective fluid modulus and effective fluid viscosity of multiphase immiscible fluids by taking into account the capillary pressure, reservoir wettability, and relative permeability simultaneously. Then, we computed the frequency-dependent velocity and inverse quality factor for different fluid proportion cases by employing Chapman's elastic model and analysed the variation features of characteristic frequency and attenuation peak. Next, the seismic reflections caused by saturation variations in a porous sand rock saturated with three-phase immiscible fluids were analysed using a simple model with four layers. Finally, the log data and real field seismic data are used to validated the numerical modelling results of our work.

2. Methodology

2.1. Calculation of effective fluid modulus and effective fluid viscosity

When porous medium is saturated by two-phase immiscible fluids (e.g. gas and water), Pagageorgiou et al. (2016) assumed that the equivalent fluid pressure P is the volumetric average of the two fluid pressures, that is

$$\widehat{P} = S_{\mathbf{W}} P_{\mathbf{W}} + S_{\mathbf{g}} P_{\mathbf{g}},\tag{1}$$

where $S_{\rm w}$ and $S_{\rm g}$ are the water saturation and gas saturation, respectively. $P_{\rm w}$ and $P_{\rm g}$ are the fluid pressures of water and gas, respectively. Note that the effective fluid pressure is related to the fluid pressure of each fluid and its proportion in the pore space. However, porous rocks generally contain three types of fluids in the hydrocarbon exploration, such as oil, gas and water. Thus, we extend the Eq. (1) to the following form:

$$\widehat{P} = S_{\mathbf{W}} P_{\mathbf{W}} + S_{\mathbf{g}} P_{\mathbf{g}} + S_{\mathbf{o}} P_{\mathbf{o}}, \tag{2}$$

where S_0 and P_0 are the saturation and fluid pressure of oil, respectively.

Since gas is usually the nonwetting phase in most cases, in our study, we assume that flow conditions of three-phase fluids are considered solely a perfect water-wet system, where water flows in contact with the pore wall, gas occupies the center of the pore and oil is the intermediate wettability phase.

Pagageorgiou et al. (2016) established the relationship between the two fluids by introducing a parameter α which can parametrize capillary pressure by scaling it to the ratio of fluid moduli. Besides, the parameter can be calculated use the model proposed by Santos et al. (1990).

We further use three parameters α_1 , α_2 and α_3 to link the relationship of any two fluid pressures. The expressions can be written as

$$P_{g} = \alpha_{1} \frac{K_{g}}{K_{o}} P_{o}; \quad P_{o} = \alpha_{2} \frac{K_{o}}{K_{w}} P_{w}; \quad P_{g} = \alpha_{3} \frac{K_{g}}{K_{w}} P_{w},$$
 (3)

where K_0 , K_g and K_w are the fluid modulus of oil, gas and water, respectively. Since the three parameters depend on the change of capillary pressures from equilibrium which in turn depend on the specific fluid distribution in the pores, we feel justified in not fixing these parameters. Thus, α_1 , α_2 and α_3 meet the following conditions:

$$1 \leq \alpha_1 \leq \alpha_{10}; \quad 1 \leq \alpha_2 \leq \alpha_{20}; \quad 1 \leq \alpha_3 \leq \alpha_{30}; \quad \alpha_3 = \alpha_1 \alpha_2, \tag{4}$$

where $\alpha_{10} = \frac{K_0}{K_\sigma}$, $\alpha_{20} = \frac{K_w}{K_0}$, $\alpha_{30} = \frac{K_w}{K_\sigma}$.

By substituting Eq. (3) into Eq. (2) the following can be obtained:

$$\widehat{P} = P_{\mathbf{W}} \left[S_{\mathbf{W}} + \alpha_2 S_{\mathbf{0}} \frac{K_{\mathbf{0}}}{K_{\mathbf{W}}} + \alpha_3 S_{\mathbf{g}} \frac{K_{\mathbf{g}}}{K_{\mathbf{W}}} \right]$$
 (5)

Eq. (5) shows the effective fluid pressure, which balances the stress at the inclusion level, is the volumetric average of the water, gas and oil fluid pressures, and is related to the interaction force between each fluid. Thus, this theory reduces to Gassmann's theory with an effective fluid modulus \widehat{K}_f given by

$$\frac{S_{\rm w}}{K_{\rm w}}P_{\rm w} + \frac{S_{\rm g}}{K_{\rm g}}P_{\rm g} + \frac{S_{\rm o}}{K_{\rm o}}P_{\rm o} = \frac{\widehat{P}}{\widehat{K}_{\rm f}}$$
 (6)

According to the Eq. (6), we can obtain:

$$\widehat{K}_{f} = \frac{\widehat{P}K_{W}K_{g}K_{o}}{S_{W}P_{W}K_{g}K_{o} + S_{o}P_{g}K_{W}K_{g} + S_{g}P_{g}K_{W}K_{o}}$$

$$\tag{7}$$

Then, by substituting Eq. (3) into Eq. (7), the $\widehat{K}_{\rm f}$ can be rewritten as

$$\widehat{K}_{f} = \frac{\widehat{P}K_{W}}{S_{W}P_{W} + \alpha_{2}S_{o}P_{W} + \alpha_{3}S_{g}P_{W}}$$
(8)

Next, by substituting Eq. (5) into Eq. (8), the expression of the central result of our paper is

$$\widehat{K}_{f} = \frac{S_{W}K_{W} + \alpha_{2}S_{o}K_{o} + \alpha_{3}S_{g}K_{g}}{S_{W} + \alpha_{2}S_{o} + \alpha_{3}S_{g}}$$

$$(9)$$

Eq. (9) provides a fluid mixing law involving two free parameters α_2 and α_3 that are associated with the capillary pressure via Eq. (3) and it reduces to Voigt average when α_2 and α_3 are both 1 and Reuss average when $\alpha_2 = \alpha_{20}$, $\alpha_3 = \alpha_{30}$ (Mavko et al., 2009). Besides, when the saturation of any each fluid is 0, Eq. (9) reduces to the expression proposed by Pagageorgiou et al. (2016).

Besides, the expression of the effective fluid viscosity η_f when porous rock saturated with two-phase immiscible fluids is (Jin et al., 2018)

$$\frac{1}{\eta_{\rm f}} = \frac{1}{\widehat{q}} \left(\frac{k_{\rm r,w}}{\eta_{\rm w}} + \frac{\alpha k_{\rm r,g}}{\eta_{\rm o}} \right),\tag{10}$$

where $\widehat{q} = S_{\rm W} + \alpha S_{\rm g}$, $1 \le \alpha \le \frac{K_{\rm w}}{K_{\rm g}}$, $k_{\rm r,w}$ and $k_{\rm r,g}$ are the relative permeability of water and gas, respectively. $\eta_{\rm W}$ and $\eta_{\rm g}$ are the dynamic viscosity of water and gas, respectively.

Then, we further extend Eq. (10) to the following form when a porous rock saturated with three-phase immiscible fluids:

$$\frac{1}{\eta_{\rm f}} = \frac{1}{\widehat{q}} \left(\frac{k_{\rm r,w}}{\eta_{\rm w}} + \frac{\alpha_2 k_{\rm r,o}}{\eta_{\rm o}} + \frac{\alpha_3 k_{\rm r,g}}{\eta_{\rm g}} \right),\tag{11}$$

where $\hat{q} = S_W + \alpha_2 S_0 + \alpha_3 S_g$, $k_{r,o}$ and η_o are the relative permeability and dynamic viscosity of oil, respectively.

The Eq. (11) can be rewritten as

$$\eta_{\rm f} = \frac{\eta_{\rm w} \eta_{\rm o} \eta_{\rm g} \left(S_{\rm w} K_{\rm w} + \alpha_2 K_{\rm o} S_{\rm o} + \alpha_3 K_{\rm g} S_{\rm g} \right)}{K_{\rm w} k_{\rm r,w} \eta_{\rm o} \eta_{\rm g} + \alpha_2 K_{\rm o} k_{\rm r,o} \eta_{\rm w} \eta_{\rm g} + \alpha_3 K_{\rm g} k_{\rm r,g} \eta_{\rm w} \eta_{\rm o}}. \tag{12}$$

Eq. (12) is the expression of the central result of effective fluid

viscosity in our study. Besides, when the saturation and relative permeability of any each fluid are 0, Eq. (12) is equivalent to Eq. (10). Eq. (12) indicates that effective fluid viscosity both depend on the relative permeability, capillary parameter, fluid viscosity and bulk modulus of each fluid.

According to the assumption about the three-phase flow conditions considered only a perfect water-wet system, the calculation of relative permeabilities are using the following expression proposed by (Bianchi Janetti et al., 2016)

$$k_{r,g} = S_g \left[S_g + 2\eta_g \left(\frac{S_W}{\mu_W} + \frac{S_0}{\mu_0} \right) \right]$$

$$k_{r,o} = S_o \left(2\frac{\eta_0}{\eta_W} S_W + S_0 \right)$$

$$k_{r,w} = S_w^2$$

$$(13)$$

Eq. (13) illustrates that the relative permeability is not only related to saturation but also depends on viscosity ratio. Notwithstanding, the relative permeability is often considered as a function solely related to saturation when analyzing dispersive effects (Papageorgiou and Chapman, 2017; Jin et al., 2018). Therefore, the relative permeability model used in the study is more suitable for the case of porous rock saturated with multiphase immiscible fluids.

2.2. Calculation of frequency-dependent velocity and attenuation

Chapman et al. (2003) proposed an anisotropic poroelastic model for fractured porous rock based on the squirt-flow mechanism. The model considers the contributions of the spherical pores, grain-scale cracks, and a set of fractures to the frequency-dependent effective stiffness tensor. The element of the effective stiffness tensor C_{iikl} can take the form:

$$C_{iikl}(\omega) = C_{iikl}^{0} - \phi_{D}C_{iikl}^{1}(\omega) - \varepsilon_{C}C_{iikl}^{2}(\omega) - \varepsilon_{f}C_{iikl}^{3}(\omega), \tag{14}$$

where C^0 is the isotropic elastic tensor of the stiffness matrix related to the Lamé parameters λ and μ . The corrections C^1 , C^2 , and C^3 are associated with the frequency, fluid type, Lamé parameters, fracture length, relaxation time parameter τ , and scaled by porosity ϕ_p , microcrack density ε_c and fracture density ε_f , respectively.

The model takes into account the fact that the fluid flow happens at both the grain scale related to the pores and microcracks and fracture scale. The two scales produce two relaxation times (or characteristic frequencies). The two relaxation times are linked by two parameters and can be represented by the following form:

$$\tau_{\rm f} = \frac{a_{\rm f}}{\varsigma} \tau_{\rm m},\tag{15}$$

where ς is the grain size, a_f is the fracture radius, τ_m is relaxation time at the grain scale while τ_f is the larger relaxation time associated with the fracture scale. The approximate expression of τ_m is given by Chapman et al. (2002):

$$\frac{1}{\tau_{\rm m}} = \frac{9\varsigma\mu}{4a^3(1-\sigma)} \frac{k}{\eta_{\rm f}},\tag{16}$$

where a is crack radius, σ is Poisson's ratio, μ is shear modulus, η_f is dynamic fluid viscosity, and k is absolute permeability of rock. Eq. (16) illustrates that the fluid mobility associated with the fluid viscosity and permeability plays an essential role in controlling the relaxation time when other parameters of the rock matrix are fixed. Therefore, the characteristic frequency (the frequency when the

attenuation gets its maximum) is both influenced by the absolute permeability of the rock and fluid viscosity.

By substituting Eq. (11) into Eq. (16), we can obtain

$$\frac{1}{\tau_{\rm m}} = \frac{9\varsigma\mu}{4a^3(1-\delta)} \frac{k}{\widehat{q}} \left(\frac{k_{\rm r,w}}{\eta_{\rm w}} + \frac{\alpha_2 k_{\rm r,o}}{\eta_{\rm o}} + \frac{\alpha_3 k_{\rm r,g}}{\eta_{\rm g}} \right). \tag{17}$$

Eq. (17) indicates that the relaxation time is also associated with relative permeability and capillary parameter. Therefore, the characteristic frequency not only depends on the matrix properties and absolute permeability of the rock, but is also associated with capillary pressure, relative permeability, and the viscosity of each fluid when porous rock is saturated by three-phase immiscible fluids. Thus, given the strong association between the dispersion and attenuation and there parameters, it is important to explore the dispersive effects when porous rock saturated with three-phase immiscible fluids.

In this study, we mainly concentrate on analysing the frequency-dependent velocity and inverse quality factor of P-wave. The expression of the compressional velocity $v(\omega)$ related to frequency and with complex values has the following form (Mavko et al., 2009):

$$v(\omega) = \left(C_{11}\sin^2\theta + C_{33}\cos^2\theta + C_{44} + \sqrt{N}\right)^{1/2}(2\rho)^{-1/2}$$
 (18)

where

$$N = \left[(C_{11} - C_{44})\sin^2\theta - (C_{33} - C_{44})\cos^2\theta \right]^2 + (C_{13} + C_{44})^2\sin^22\theta$$
 (19)

and θ is the angle between the wave vector and the x3-axis of symmetry shown in Fig. 1 (Mavko et al., 2009). In our study, we use a fixed θ (25°) to calculate all the velocities.

According to the previous analysis, the frequency-dependent velocity $v(\omega)$ is related to multiple factors when other parameters related to porosity, cracks, and microcracks of rocks are fixed. We use the following equation to express:

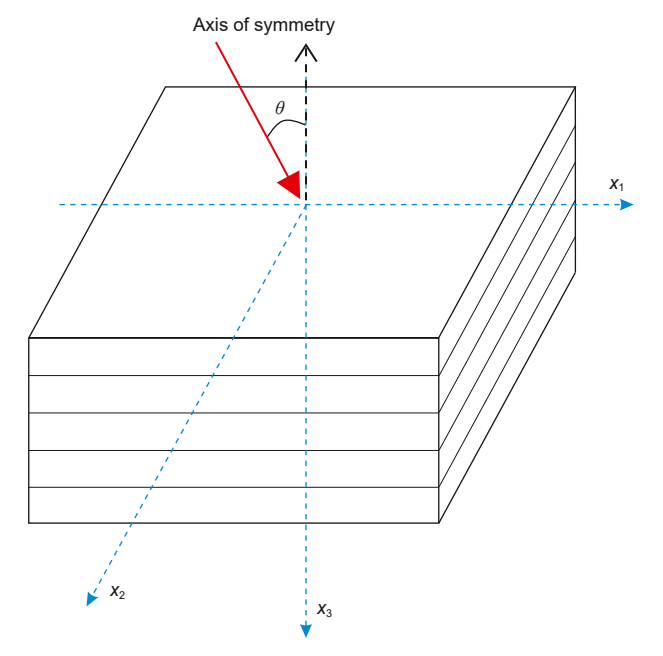


Fig. 1. A VTI medium model with angel θ and x_3 -axis of symmetry.

Table 1 Fluid parameters used in the calculations.

Properties	Oil	Gas	Water
Bulk modulus, MPa Dynamic viscosity, Pa·s	$1248.8 \\ 1.2687 \times 10^{-3}$	$60.6122 \\ 0.0254 \times 10^{-3}$	3024.4 0.755×10^{-3}

$$v(\omega) = f(S_i, \alpha_2, \alpha_3, k_{ri}), i = 0, g, w, \tag{20}$$

where S_i and k_{ri} are the saturation and relative permeability of each fluid, respectively, and the characters o, g, and w donate the oil, gas and water, respectively.

Next, the frequency-dependent velocity and inverse quality factor of P-wave can be calculated by (Rubino et al., 2012)

$$v_{p}(\omega) = \frac{1}{\text{Re}[1/\nu(\omega)]}, \frac{1}{Q_{p}(\omega)} = \frac{\text{Im}\left[\nu(\omega)^{2}\right]}{\text{Re}\left[\nu(\omega)^{2}\right]}.$$
 (21)

3. Numerical analysis

Firstly, we analyse the characteristics of the effective fluid modulus and effective fluid viscosity of three-phase immiscible fluids, and the fundamental parameters of three fluids used in the calculation are listed in Table 1. The fluid parameters are calculated by the equation of Batzle and Wang (1992) at a pressure of 25 MPa, a temperature of 50 °C, a salinity of 100,000 ppm, a density of dead oil (i.e. gas-free oil) of 750 kg/m³ and a gas to air density ratio set at 0.65. The fluid modulus ratio of any two-phase fluid can be obtained, that is, $K_{\rm W}/K_{\rm g} \approx 50$, $K_{\rm W}/K_{\rm o} \approx 50$, $K_{\rm o}/K_{\rm g} \approx 20.6$.

3.1. The analysis of effective fluid modulus

Eq. (12) indicates that the effective fluid modulus is related to the parameters α_2 and α_3 for the three-phase immiscible fluids. Here, we analyse the effective fluid modulus under the case of the

two parameters given different values. Fig. 2 shows the distribution results of effective fluid modulus when α_3 given six different values and $\alpha_2=1$. It can be seen that the larger values are gathers to the lower left corner of the triangle plane, that is, it moves toward the direction of lower gas saturation and higher water saturation. Meanwhile, the lower values are focused on the zone with higher gas saturation and lower oil saturation. Besides, for the α_3 increasing, the distribution characteristics show obvious changes. Fig. 3 shows the distribution results of effective fluid modulus when α_3 given six different values and $\alpha_2=\alpha_{20}$. The results demonstrate that the variation characteristics of the effective fluid modulus are similar to those seen in Fig. 2. The primary cause of this phenomenon is because the bulk modulus ratio of oil and water is small, in turn resulting in a small difference between $\alpha_2=1$ and $\alpha_2=\alpha_{20}$.

Then, the distribution results of effective fluid modulus when α_2 given six different values and $\alpha_3 = 1$ are analysed in Fig. 4. It can be observed in Fig. 4(a)–(f) that the larger values are also gathered in the bottom-left zone with higher water saturation and lower gas saturation while the lower values are mainly gathered in the upperright part of the triangle plane. However, the distribution characteristics of effective fluid modulus for different α_2 are similar because of the small variation range of α_2 . Besides, the effective fluid modulus increases approximately linearly with increasing saturation for a specific saturation state. Similarly, we analysed the distribution results of effective fluid modulus when α_2 given six different values and $\alpha_3 = \alpha_{30}$ in Fig. 5. The results indicate that the effective fluid modulus varies nonlinearly with gas saturation and oil saturation and the trend of change is more intense in the range of lower gas saturation and higher water saturation, as well as in the range of lower water saturation and higher oil saturation. Besides, the distribution characteristics of effective fluid modulus for different α_2 in Fig. 4(a)–(f) are similar and the same characteristics are shown in Fig. 5(a)–(f). The primary cause of this phenomenon is the small variation range of α_2 , resulting in a small difference in effective fluid modulus when α_3 is fixed.

To sum up, the effective fluid modulus of three immiscible fluids is more affected by α_3 , that is, the bulk modulus ratio of water and gas has a significant impact on the effective fluid modulus of three

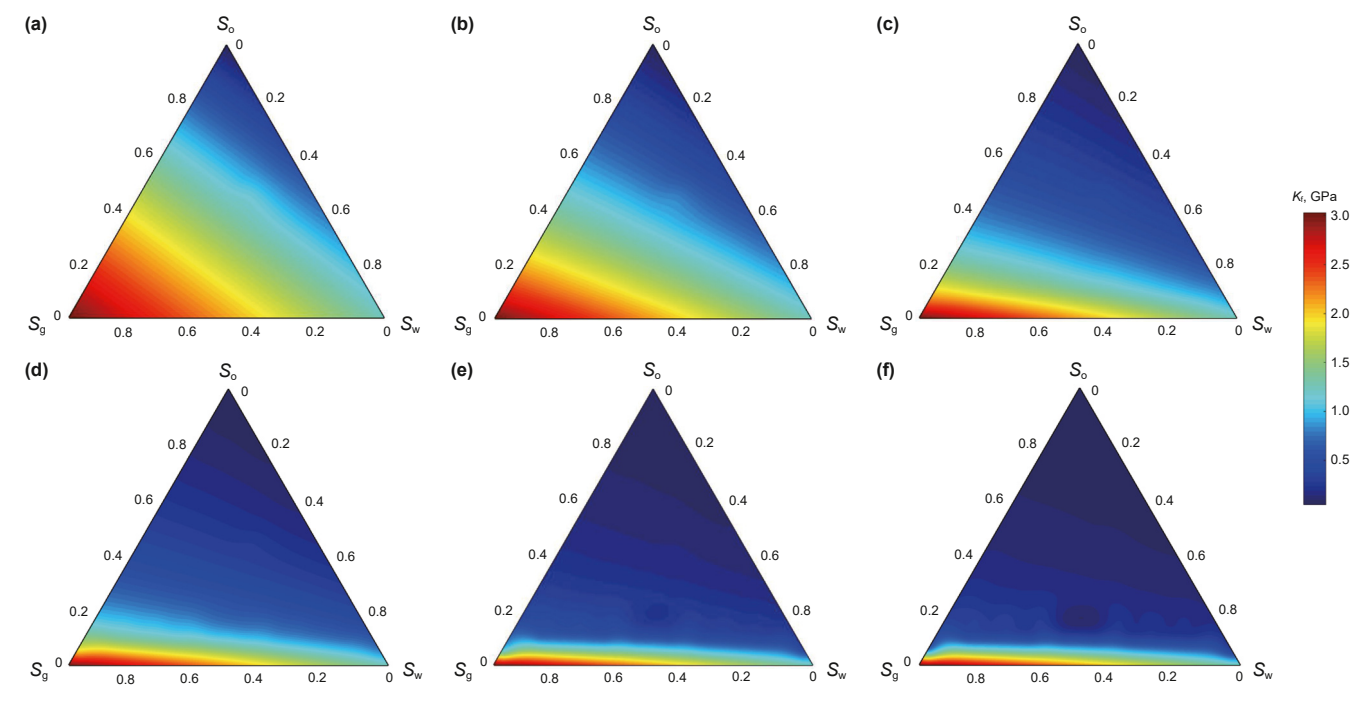


Fig. 2. The distribution results of effective fluid modulus when α_3 given six different values and $\alpha_2 = 1$. (a) $\alpha_3 = 1$; (b) $\alpha_3 = 2$; (c) $\alpha_3 = 5$; (d) $\alpha_3 = 10$; (e) $\alpha_3 = 30$; (f) $\alpha_3 = \alpha_{30}$.

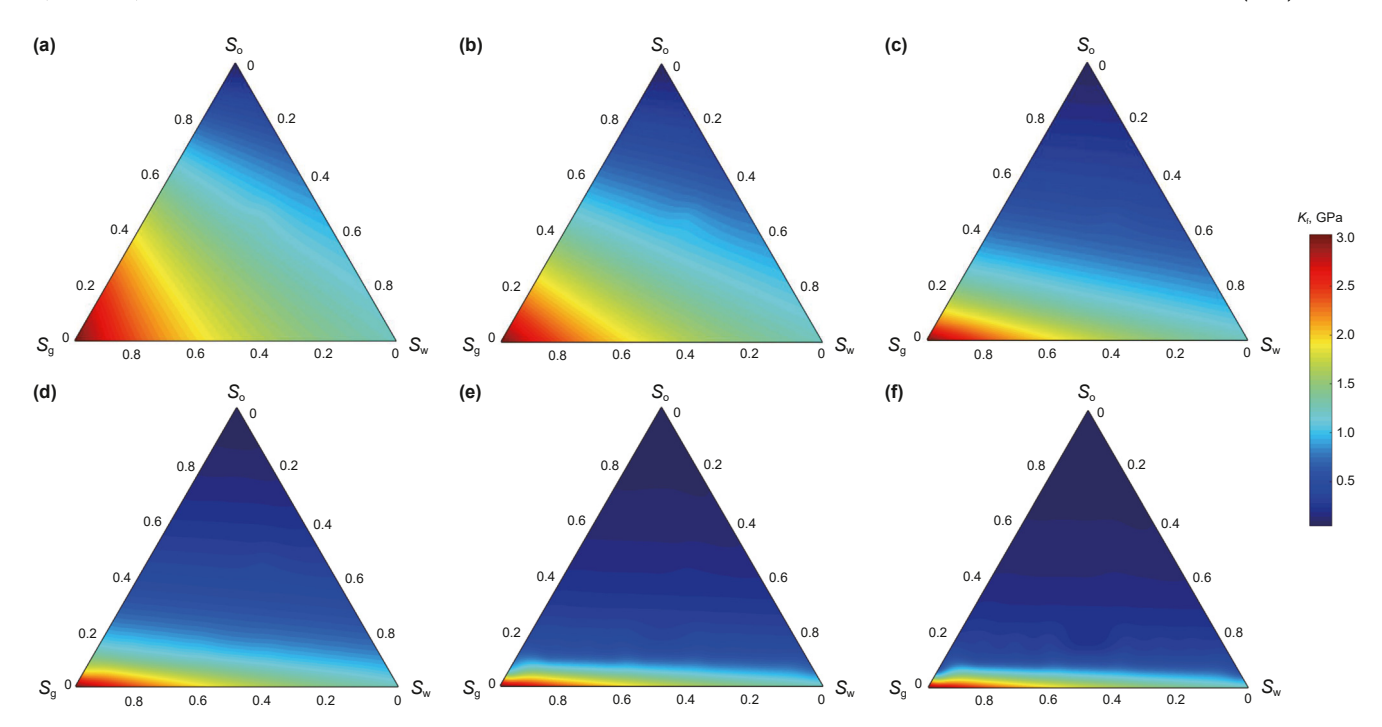


Fig. 3. The distribution results of effective fluid modulus when α_3 given six different values and $\alpha_2 = \alpha_{20}$. (a) $\alpha_3 = 1$; (b) $\alpha_3 = 2$; (c) $\alpha_3 = 5$; (d) $\alpha_3 = 10$; (e) $\alpha_3 = 30$; (f) $\alpha_3 = \alpha_{30}$.

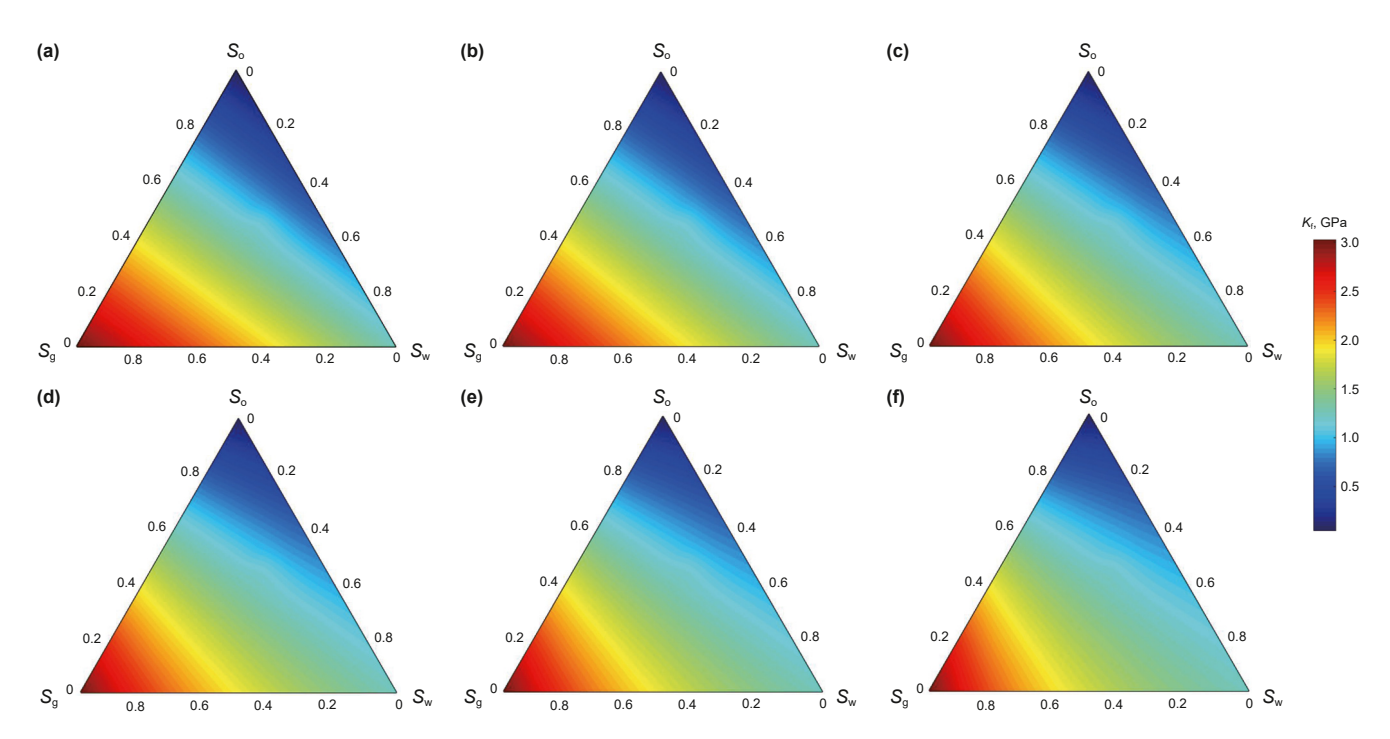


Fig. 4. The distribution results of effective fluid modulus when α_2 given six different values and $\alpha_3 = 1$. (a) $\alpha_2 = 1$; (b) $\alpha_2 = 1.2$; (c) $\alpha_2 = 1.5$; (d) $\alpha_2 = 1.8$; (e) $\alpha_2 = 2$; (f) $\alpha_2 = \alpha_{20}$.

immiscible fluids. In addition, the larger difference in fluid modulus between wetting phase and nonwetting phase results in the greater difference in capillary pressure, which in turn affects the distribution of the fluid and makes the greater change in effective fluid modulus.

3.2. The analysis of effective fluid viscosity

Eq. (15) indicates that the relative permeability of each fluid plays a significant role to the effective fluid viscosity. We first analyse the characteristics of the relative permeability of each fluid

in Fig. 6. The results illustrate that the relative permeability of the gas and water are less than 1 (Fig. 6(a)–(c)). However, the relative permeability of oil is greater than 1 under a specific saturation ratio (Fig. 6(b)) because the value is not only related to saturation and affected by the viscosity ratio of fluid (Yiotis et al., 2007; Zhao et al., 2017). The relative permeability is over than 1 because of lubricating impact (Yiotis et al., 2007; Huang and Lu, 2009) at the case of $\eta_{\rm o}/\eta_{\rm w}>1$ and the lower gas saturation, the more values are greater than 1 (Fig. 6(b)). Meanwhile, the larger values of oil relative permeability are concentrated in the range of 0.2 < $S_{\rm w}<0.5$ while

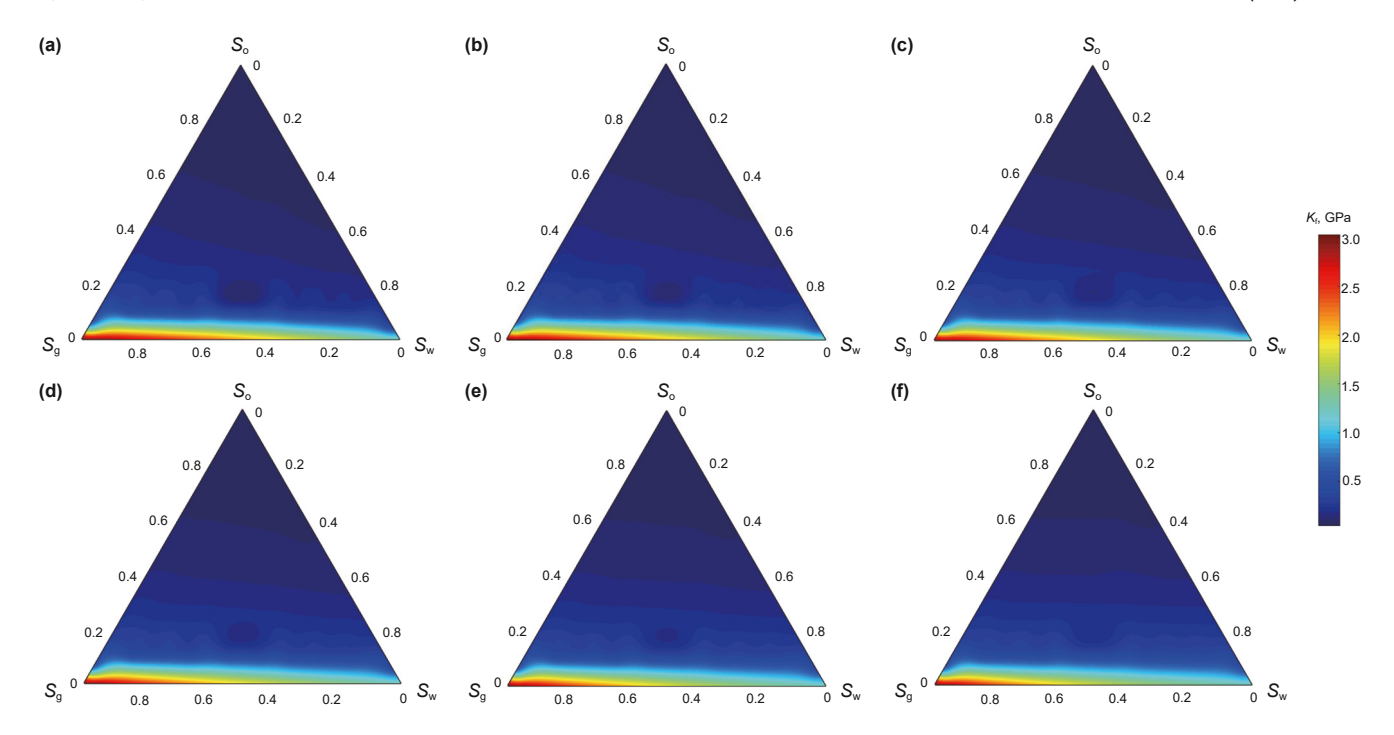


Fig. 5. The distribution results of effective fluid modulus when α_2 given six different values and $\alpha_3 = \alpha_{30}$. (a) $\alpha_2 = 1$; (b) $\alpha_2 = 1.2$; (c) $\alpha_2 = 1.5$; (d) $\alpha_2 = 1.8$; (e) $\alpha_2 = 2$; (f) $\alpha_2 = \alpha_{20}$.

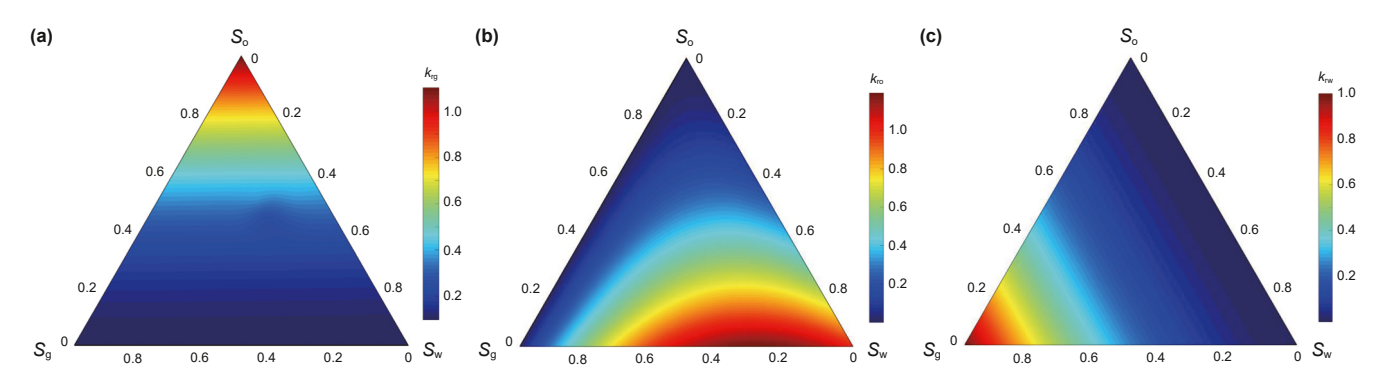


Fig. 6. Relative permeabilities of (a) gas, (b) oil and (c) water for a rock saturated by three-phase immiscible fluids.

the maximum relative permeabilities of gas and water are 1 when $S_0 = 0$, $S_g = 1$ and $S_0 = 0$, $S_w = 1$, respectively.

Then, we analyse the effective fluid viscosity under the case of the two parameters α_2 and α_3 given different values. Fig. 7 shows the distribution results of effective fluid viscosity when α_3 given six different values and $\alpha_2 = 1$. The results indicate that the larger values are gathered in the lower right corner of the triangular plane and the maximum for different parameters conditions are equal to the oil viscosity. However, the maximum value moves towards the direction of increasing oil saturation and decreasing water saturation. Besides, the nonlinerity between effective fluid viscosity and saturation is stronger in the case of oil and water, and oil and gas, while the effective fluid viscosity gradually decreases with water saturation increasing in the case of gas and water. The distribution results (Fig. 8) of effective fluid modulus when α_3 given six different values and $\alpha_2 = \alpha_{20}$ illustrates that the variation characteristic is similar to Fig. 7 when α_3 increases. However, it is worth noting that the maximum effective fluid viscosity when α_3 given different values. The maximum effective fluid viscosity gets its maximum when α_3 is 1 and its decreases with α_3 increasing. To observe the variation in effective fluid viscosity as it gets its maximum value

when α_3 increases more clearly, the curve for α_3 corresponding to the maximum fluid viscosity is selected for further analysis in Fig. 9. Note that the maximum effective fluid viscosity is 1.522 cP when α_3 is 1 and then its decreases nonlinearly as α_3 increases from 1 to 13.95. This decreasing tendency is more pronounced for smaller α_3 parameters, and it begins to slow as the α_3 increases to 13.95. For the $\alpha_3 > 13.95$, the maximum effective fluid viscosity is a constant value (1.2678 cP, the oil viscosity).

Further, we also analysed the effective fluid viscosity when α_2 given six different values and $\alpha_3=1$ in Fig. 10. Note that the larger values are mainly gathered in the zone of larger oil saturation and smaller water saturation and the effective fluid viscosity will get its maximum value at a specific ratio of oil and gas while its maximum for different α_2 is different. To comparatively analyse the variation characteristics of the maximum value of effective fluid viscosity corresponding to Fig. 10, the curve of maximum fluid viscosity when $\alpha_3=1$ variation with the α_2 is picked (Fig. 11) and the results show that the maximum fluid viscosity increases approximately linearly from 1.3778 cP to 1.522 cP with the α_2 increases. Besides, Fig. 10 exhibits distinctive variation characteristics that have a small difference when α_2 increases when compared with the previous

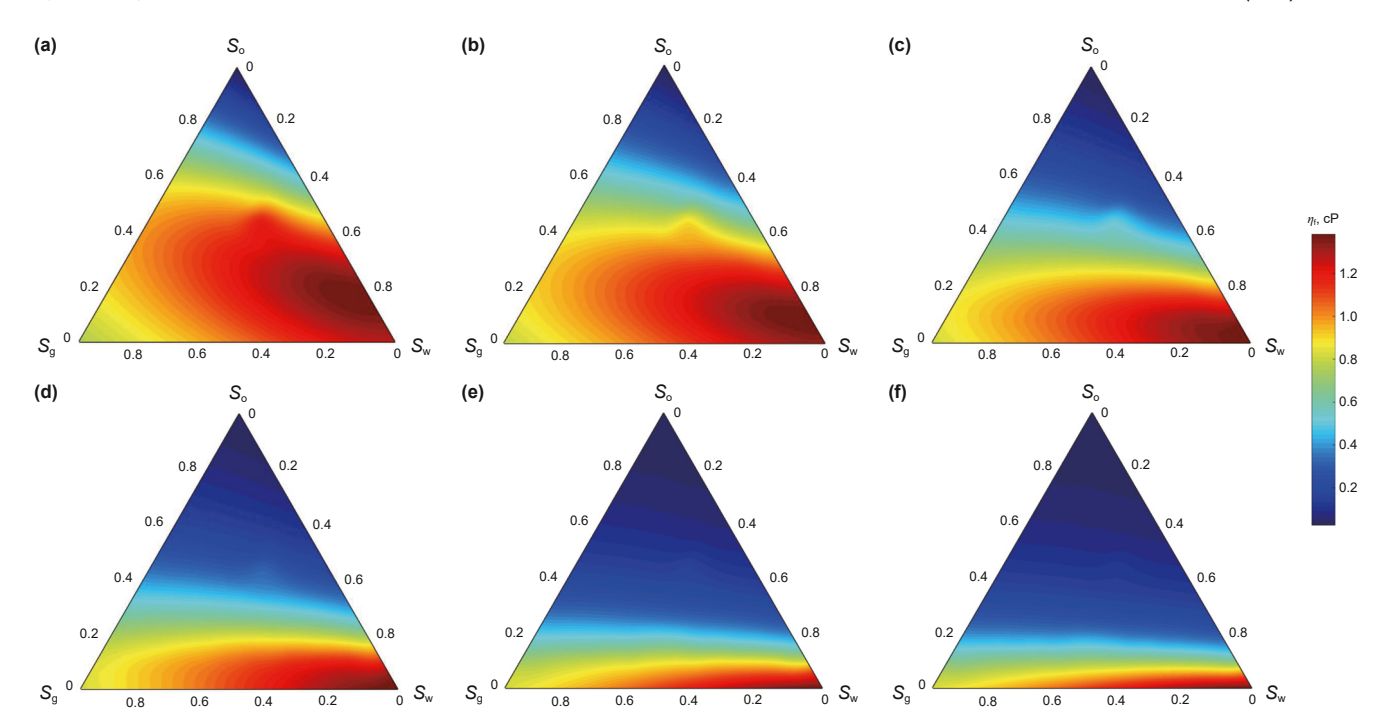


Fig. 7. The distribution results of effective fluid viscosity when α_3 given six different values and $\alpha_2 = 1$. (a) $\alpha_3 = 1$; (b) $\alpha_3 = 2$; (c) $\alpha_3 = 5$; (d) $\alpha_3 = 10$; (e) $\alpha_3 = 30$; (f) $\alpha_3 = \alpha_{30}$.

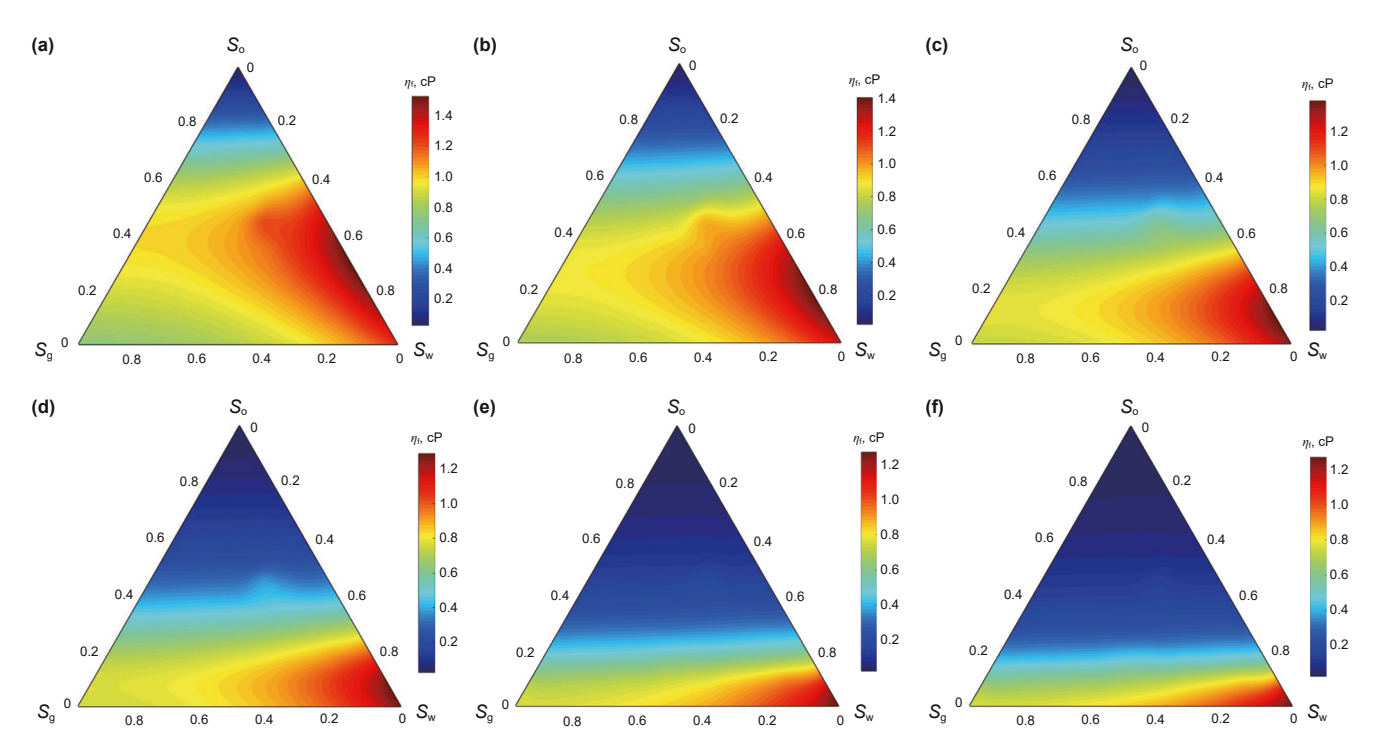


Fig. 8. The distribution results of effective fluid viscosity when α_3 given six different values and $\alpha_2 = \alpha_{20}$. (a) $\alpha_3 = 1$; (b) $\alpha_3 = 2$; (c) $\alpha_3 = 5$; (d) $\alpha_3 = 10$; (e) $\alpha_3 = 30$; (f) $\alpha_3 = \alpha_{30}$.

two cases in Figs. 7 and 8, while the variation characteristics of the subgraphs shown in Figs. 7 and 8 have a larger difference when α_3 increases, which indicates that the small range of α_2 results in a little influence for effective fluid viscosity. The distribution results of effective fluid viscosity when α_2 given six different values and $\alpha_3 = \alpha_{30}$ shown in Fig. 12 illustrates that the variation characteristics of the subgraphs is similar and the maximum value for different α_2 is same (equal to the oil viscosity). However, the

effective fluid viscosity above the four cases (Figs. 7, 8, 10 and 12) all gets the same minimum value under fully gas saturated conditions, that is the gas viscosity.

To sum up, the effective fluid viscosity of three immiscible fluids is significantly affected by capillary parameter α_3 , and it will get a larger value that is greater than the respective viscosity of three fluids due to the effect of relative permeability.

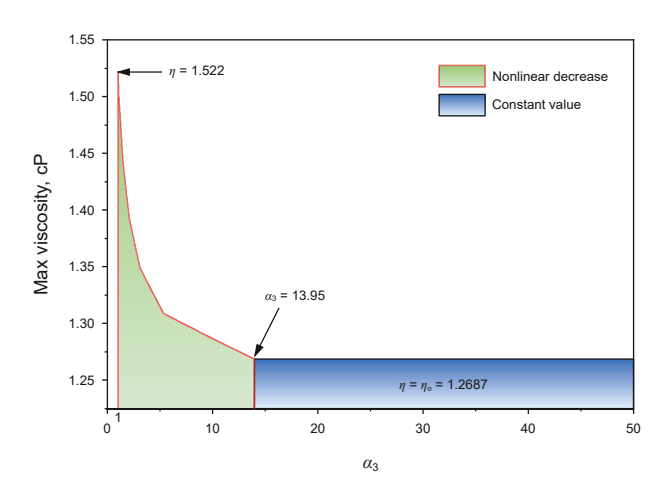


Fig. 9. The variation of the maximum effective fluid viscosity with α_3 when $\alpha_2 = \alpha_{20}$.

3.3. The analysis of dispersion and attenuation

Using the poroelastic theory of Chapman model (Chapman et al., 2003) as a guide, the frequency-dependent velocities and inverse quality factors of porous rocks saturated with three-phase immiscible fluids are calculated to analyse the characteristics of the dispersion and attenuation. Table 2 lists the rock parameters, which are referenced the values of the data derived from the sandstone sample of Rathore et al. (1995). The velocities are measured in the state of the sandstone sample is water-saturated. We consider three cases where porous rock is saturated by three-phase immiscible fluids: water, oil and gas where the ratio of oil and gas is 1:1 (e.g. when the water saturation is 0.6, the oil and gas saturation are both 0.2, their ratio is 1:1), 3:1 and 1:3, respectively. Besides, the effective fluid modulus and fluid viscosity are both significantly affected

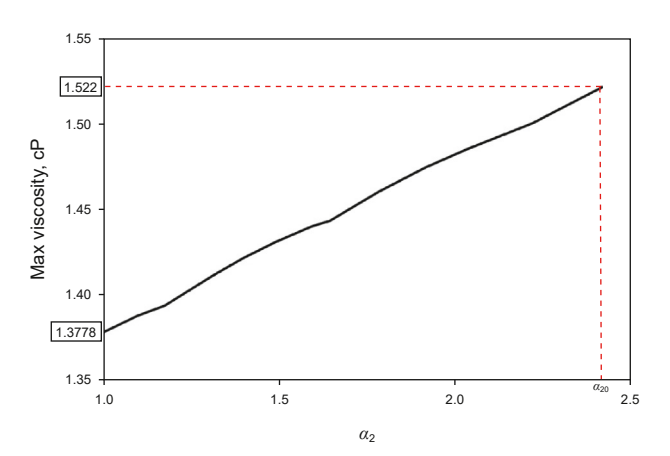


Fig. 11. The variation of the maximum effective fluid viscosity with α_2 when $\alpha_3 = 1$.

by the parameter α_3 while have a small difference for different α_2 according to the analysis in Sections 3.1 and 3.2. Thus, to simplify the analysis, numerical analysis is conducted when α_3 given six different values and α_2 is fixed to 1.

3.3.1. The saturation ratio of oil and gas is 1:1

For the case of the rock saturated with water, oil and gas and the ratio of the oil and gas is 1:1, the relative permeability curves are shown in Fig. 13. Fig. 14(a) indicates that the effective fluid modulus is increases linearly with $S_{\rm w}$ increasing when α_2 is 1 which is same with the result of Voigt average. However, the increasing trend is nonlinear when α_3 is greater than 1 and it becomes severe as α_3 increases. The maximum effective fluid modulus for all different parameters is equal to the bulk modulus of water ($S_{\rm w}=1$). In Fig. 14(b), the variation characteristic of effective fluid viscosity is different for different α_3 which suggests that flow of the viscous pore fluid is significantly affected by capillary parameter and fluid

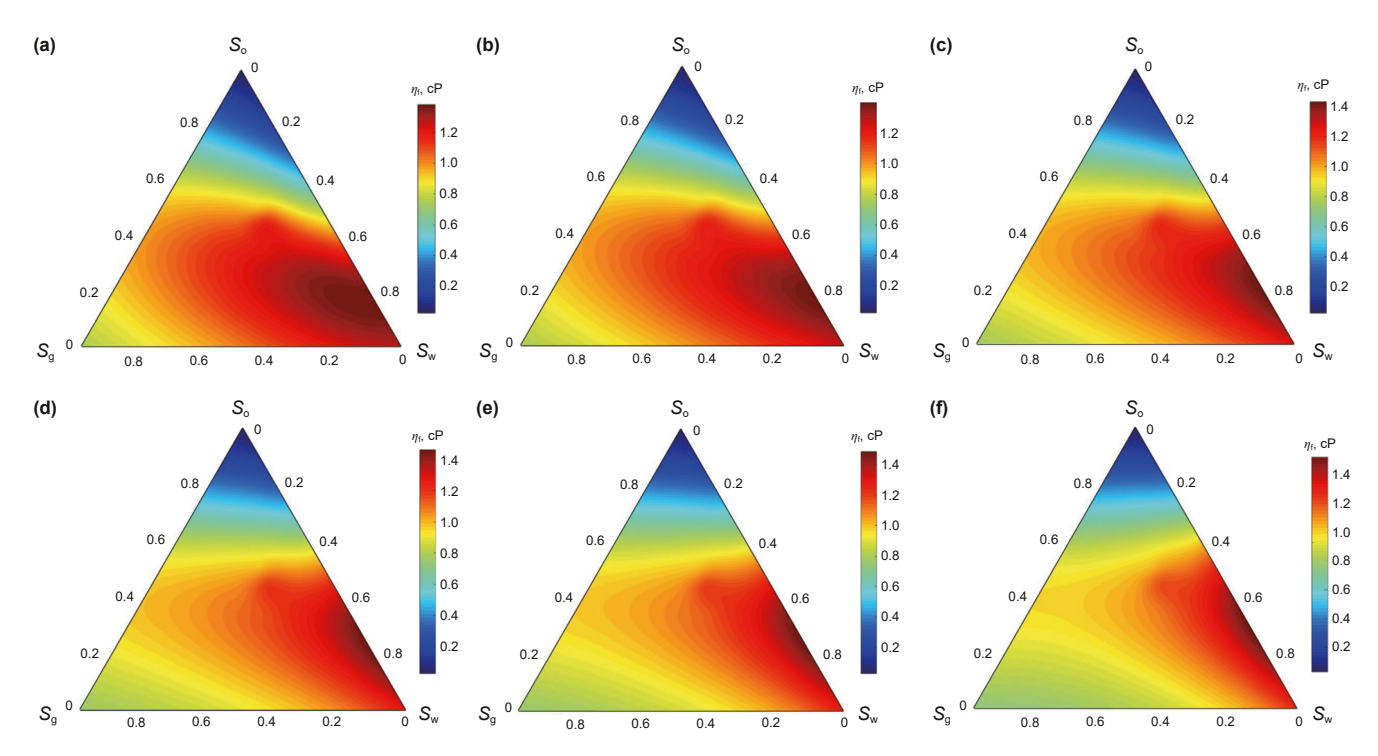


Fig. 10. The distribution results of effective fluid viscosity when α_3 given six different values and $\alpha_3 = 1$. (a) $\alpha_2 = 1$; (b) $\alpha_2 = 1.2$; (c) $\alpha_2 = 1.5$; (d) $\alpha_2 = 1.8$; (e) $\alpha_2 = 2$; (f) $\alpha_2 = \alpha_{20}$.



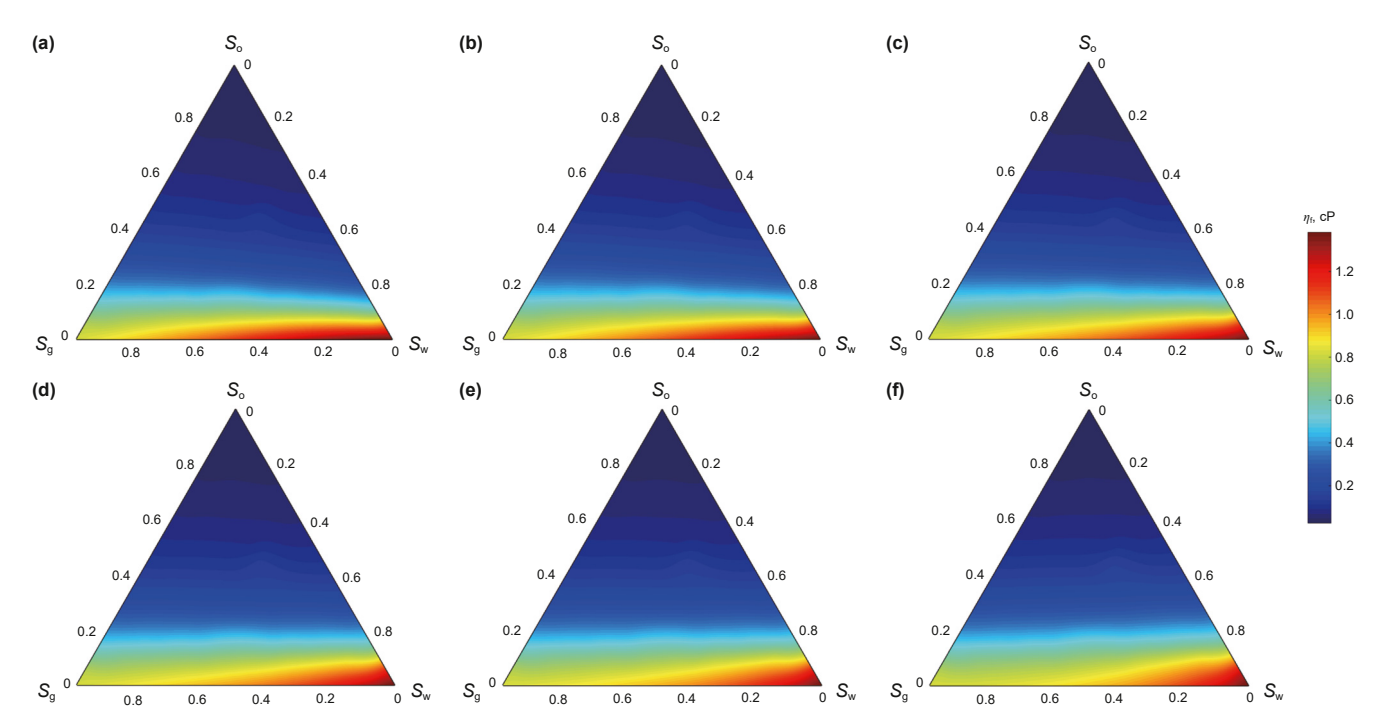


Fig. 12. The distribution results of effective fluid viscosity when α_3 given six different values and $\alpha_3 = \alpha_{30}$. (a) $\alpha_2 = 1$; (b) $\alpha_2 = 1.2$; (c) $\alpha_2 = 1.5$; (d) $\alpha_2 = 1.5$; (e) $\alpha_2 = 2$; (f) $\alpha_2 = \alpha_{20}$.

Table 2 Parameters of the porous rock.

Properties	Value
Reference P-wave velocity, m/s	2678
Reference S-wave velocity, m/s	1384
Matrix density, kg/m ³	1712
Grain size, m	0.001
Porosity, %	15
Fracture radius, m	0.5
Micro-crack radius, mm	2.75
Aspect ratio	0.0036
Fracture density	0.001
Micro-crack density	0.1

content. For the case of $\alpha_3 = \alpha_{30}$, the effective viscosity increases as water saturation increases, which indicates that the flowability of the fluids decreases with increasing water proportion. Note that for

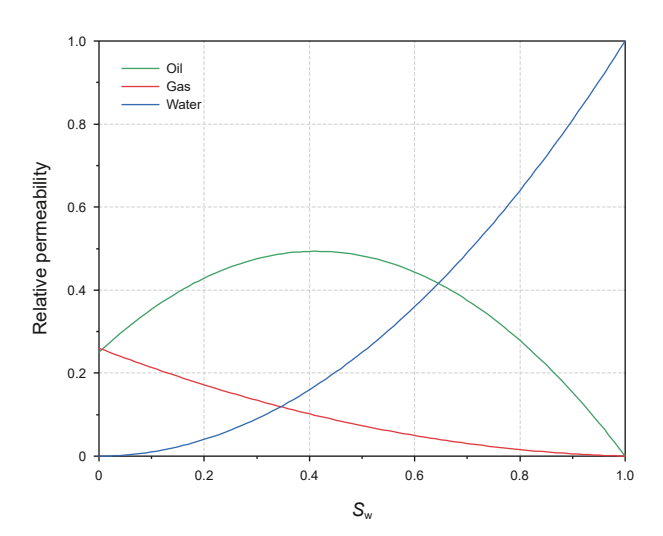


Fig. 13. Relative permeabilities of the rock saturated with water, oil and gas (the ratio of the oil and gas is 1:1).

different parameters α_3 , the effective viscosity is same when the $S_{\rm W}=1$.

Fig. 15 shows the 2D distributions of frequency-dependent velocities at six specific α_3 . It can be observed that the frequencydependent velocities increase with water saturation for different α_3 while the dispersion features show a distinct tendency. In Fig. 16, the 2D distributions of frequency-dependent attenuation at six specific α_3 show that the attenuation peak at a specific α_3 changes non-linearly with water saturation and the maximum attenuation peak of the 2D plane moves towards the direction of larger water saturation as α_3 increases. We further investigate the features of the attenuation peaks and characteristic frequencies in relation to water saturation (S_w) at six assigned parameter α_3 values when $\alpha_2 = 1$ in Fig. 17. Fig. 17(a) shows that the attenuation peaks approximately linearly decrease with increasing S_w when $\alpha_3 < 5$ and reaches its maximum value when S_w is 0. It is worth noting that the nonlinearity is enhanced as α_3 increases when $\alpha_3 \geq 5$ and the maximum attenuation gets the peak value at a particular water saturation and then decreases with the S_w increasing. However, the maximum attenuation value is the same when the rock is fully saturated with water because this situation is a signal fluid that is not affected by fluid pressure between fluids. As shown in Fig. 17(b), the characteristic frequency nonlinearly changes as the S_{w} increases. Note that the characteristic frequency first decreases with increasing S_w and reaches a minimum value at a particular S_w and then it slightly increases to a same value as S_{W} increases to 1 within a lower seismic frequency range. In addition, the characteristic frequency will be within a narrower frequency band range for a smaller α_3 and all lies in the frequency band of seismic exploration when $\alpha_3 = 1$. Moreover, the characteristic frequency could also occur in a lower range of frequency band for a higher $S_{\rm W}$ and $\alpha_{\rm 3}$, which indicates that the dispersion and attenuation within the seismic frequency range are both influenced by capillary parameter and wetting phase saturation.

3.3.2. The saturation ratio of oil and gas is 1:3

For the case of the rock saturated with water, oil and gas and the ratio of the oil and gas is 1:3, the relative permeability curves are

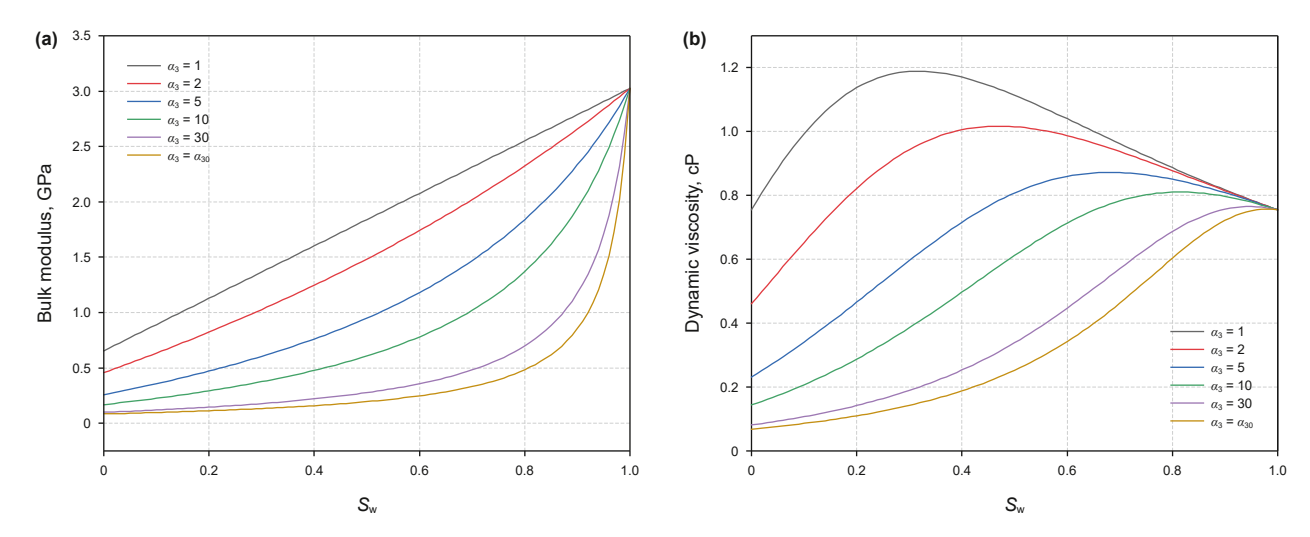


Fig. 14. The effective fluid modulus (a) and fluid viscosity (b) when α_3 given six different values and $\alpha_2 = 1$ for three-phase immiscible fluids and the ratio of the oil and gas is 1:1.

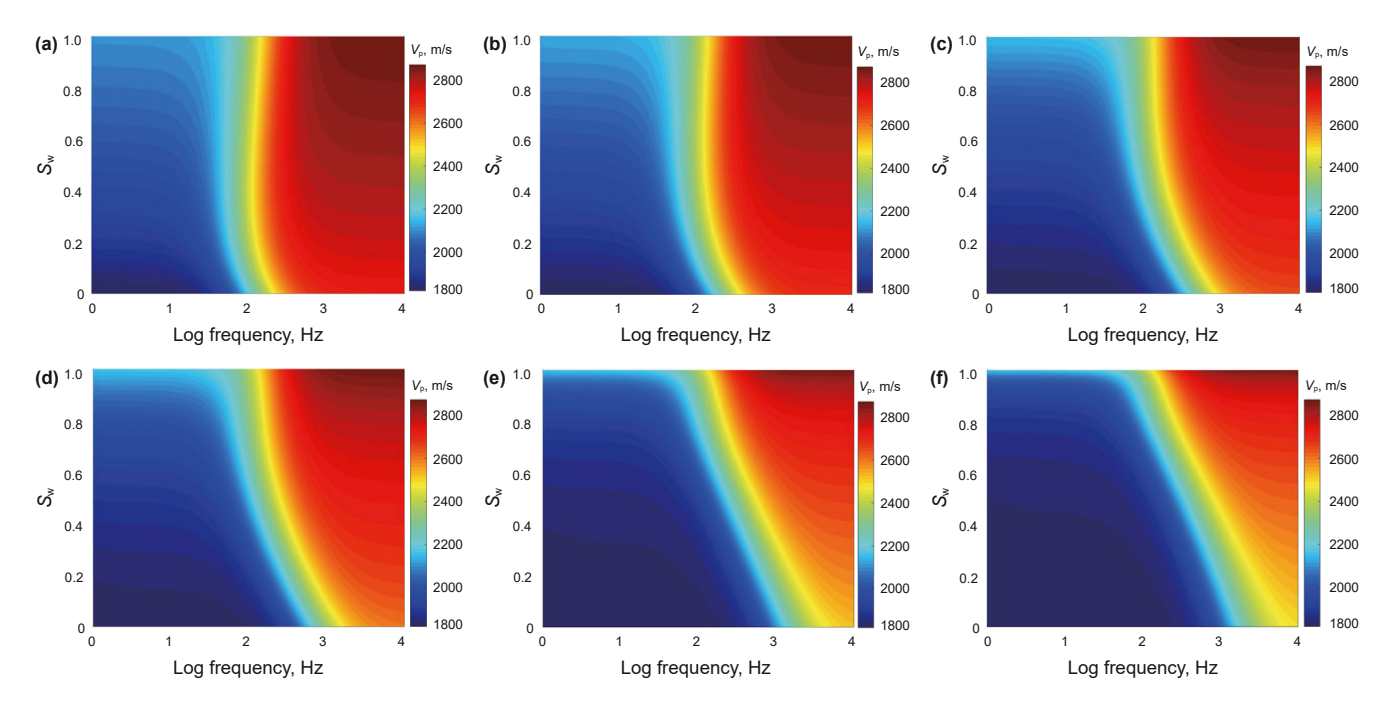


Fig. 15. The distributions of frequency-dependent velocity of P-wave on the frequency and water saturation plane when α_3 given six different values and $\alpha_2 = 1$ for the rock saturated with water, oil and gas and the ratio of the oil and gas is 1:1. (a) $\alpha_3 = 1$; (b) $\alpha_3 = 2$; (c) $\alpha_3 = 5$; (d) $\alpha_3 = 10$; (e) $\alpha_3 = 30$; (f) $\alpha_3 = \alpha_{30}$.

shown in Fig. 18. The characteristics of the effective fluid modulus in Fig. 19(a) and effective fluid viscosity in Fig. 19(b) are similar to the results seen in Fig. 14(a) and (b), respectively. However, the values in Fig. 19 are different from Fig. 14 for the same parameters except the case of $S_{\rm W}=1$.

Fig. 20 shows the 2D distributions of frequency-dependent velocities when α_3 given six different values and $\alpha_2=1$ for the rock saturated with water and oil-gas with 1:3 proportion and Fig. 21 shows the corresponding frequency-dependent attenuations. The results indicate that the distribution of the dispersion and attenuation and its variation characteristics are similar to those seen in Figs. 15 and 16 while exists small differences in the changes of attenuation peaks. In Fig. 22(a), the attenuation peak approximately linearly decreases as $S_{\rm w}$ increases only when $\alpha_3=1$ and

other attenuation peaks get the maximum value at a specific saturation when $\alpha_3 > 1$. Besides, the nonlinearity is enhanced and the specific saturation (the saturation when the attenuation peak gets its maximum value) shifts towards the larger water saturation direction as α_3 increases. The overall variation trend of characteristic frequency and water saturation shown in Fig. 22(b) is also similar to Fig. 17(b) while the frequency is higher than the case of 1.1

3.3.3. The saturation ratio of oil and gas is 3:1

For the case of the rock saturated with water, oil and gas and the ratio of the oil and gas is 3:1, It can be observed that the relative permeability of oil is significantly higher than gas (Fig. 23). The variation characteristics of the effective fluid modulus and effective

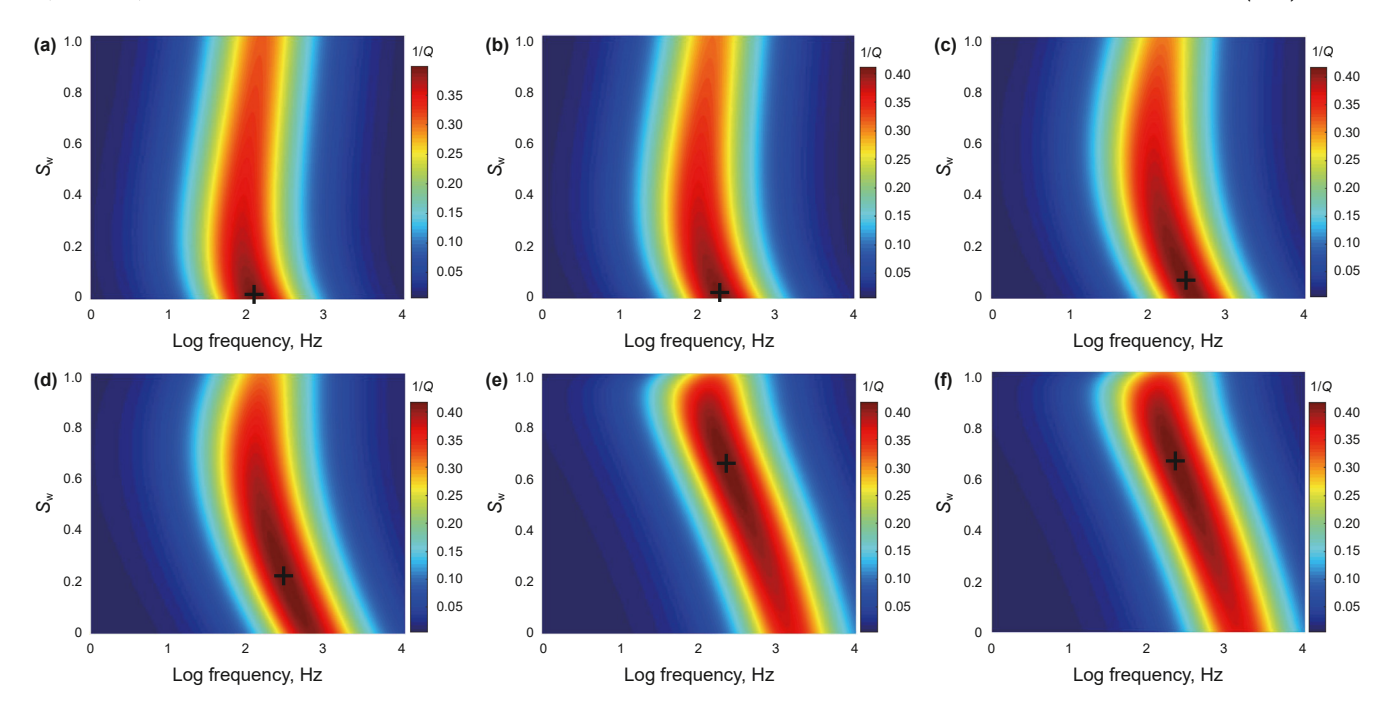


Fig. 16. The distributions of frequency-dependent inverse quality factor of P-wave on the frequency and water saturation plane when α_3 given six different values and $\alpha_2 = 1$ for the rock saturated with water, oil and gas and the ratio of the oil and gas is 1:1. (a) $\alpha_3 = 1$; (b) $\alpha_3 = 2$; (c) $\alpha_3 = 5$; (d) $\alpha_3 = 10$; (e) $\alpha_3 = 30$; (f) $\alpha_3 = \alpha_{30}$ (The symbol '+' donates the location of the maximum attenuation peak of the 2D plane).

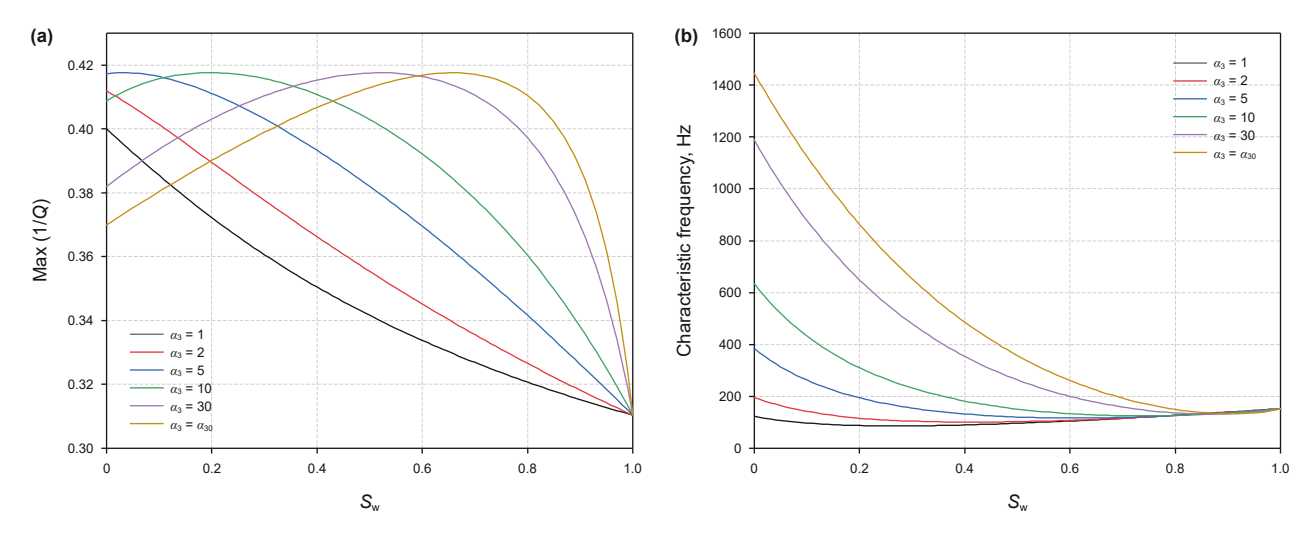


Fig. 17. (a) Attenuation peaks and (b) characteristic frequencies when α_3 given six different values and $\alpha_2 = 1$ for the rock saturated with water, oil and gas and the ratio of the oil and gas is 1:1.

fluid viscosity with the water saturation shown in Fig. 24(a) and (b) are also similar with the 1:1 case while the values at $S_{\rm W}=0$ exhibits distinct differences for different α_3 .

The 2D distributions of frequency-dependent velocities shown in Fig. 25 show that the characteristics of each subgraph have a relatively little change with the increase of α_3 compared with the previous cases in Figs. 15 and 20. Fig. 26 exhibits the corresponding frequency-dependent attenuations. It can be seen that the attenuation decreases as $S_{\rm w}$ increases at a specific frequency and gets its maximum value at the case of $S_{\rm w}=0$ when $\alpha_3<30$. However, the attenuation peak exhibits significant nonlinear characteristics as $S_{\rm w}$ changes on the 2D plane of frequency and water saturation and gets its maximum at the location of a specific water saturation and frequency when α_3 is 30 and α_{30} and these features are more distinctly

shown in Fig. 27(a). Fig. 27(b) illustrates that the characteristic frequency decreases significantly as $S_{\rm W}$ increases, reaches a minimum value at a specific $S_{\rm W}$ and then increases slowly with the increase of $S_{\rm W}$ when $\alpha_3 > 5$. When α_3 is reduced to a lower value, the characteristic frequency can be observed in a low-frequency range, even within the seismic frequency band (50–150 Hz) when $\alpha_3 \leq 5$. It can be observed that the characteristic frequency is far outside the range restriction of seismic frequency for lower wetting phase saturation values and higher values of α_3 , while it may fall inside the frequency band of seismic exploration for a higher $S_{\rm W}$ level. Besides, the variation range of characteristic frequency is narrower when the oil content increases compared with the 1:1 and 1:3 cases, indicating that dispersion and attenuation are more probably to occur in the low-frequency range.

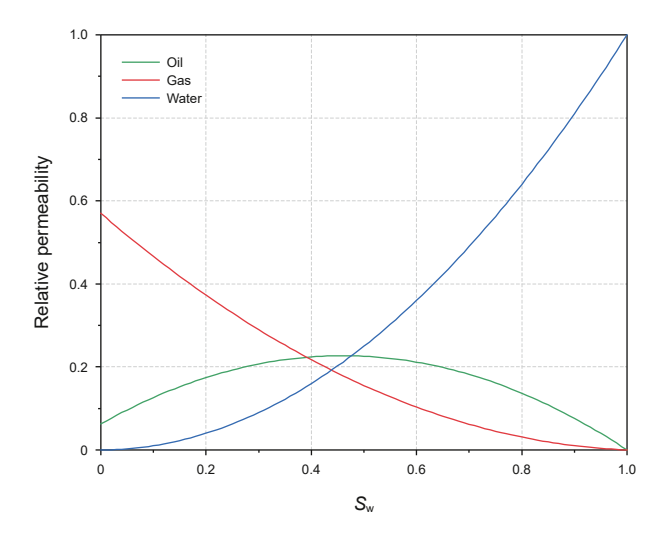


Fig. 18. Relative permeabilities of the rock saturated with water, oil and gas and the ratio of the oil and gas is 1:3.

3.4. The seismic responses analysis

3.4.1. Synthetic data analysis

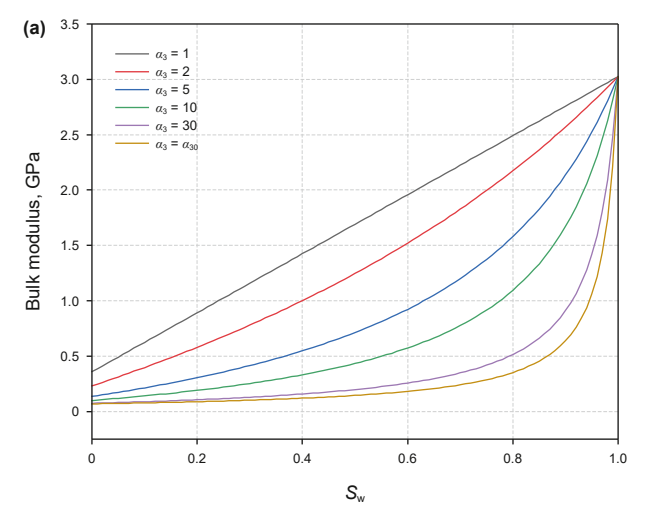
To investigate the features of the seismic reflections when seismic wave passes through a rock saturated with three-phase immiscible fluids, a simple model with four layers shown in Fig. 28 is designed to explore the seismic responses features. In the forward modeling, the phase-shifted method based on diffusive and viscous wave equation (Chen et al., 2016b) is used to generate the seismic responses. Table 3 lists the model parameters of the shales. According to the analysis results in the Section 3.3, the dispersion and attenuation are more likely to occur in lower seismic frequency band when $\alpha_2 = \alpha_3 = 1$. Therefore, in the case of $\alpha_2 = \alpha_3 = 1$, we analysis the variation of seismic responses with wetting phase saturation ($S_{\rm w}$) under the three cases of a porous rock saturated with three-phase immiscible fluids with the ratios of oil and gas are 1:1, 1:3 and 3:1, respectively.

The seismic responses of the three cases shown in Figs. 29-31 illustrate that the bottom reflections of the multiphase fluid-saturated sand rock and the last reflections of the model show significant time delay as $S_{\rm w}$ decreases when seismic wave going

through the porous medium containing fluids, which is mainly caused by the velocity increases. However, the degree of waveform distortion and energy loss are different due to the differences in velocity dispersion and attenuation. As shown in Figs. 29(a), 30(a) and 31(a), the last reflections exhibit obvious energy loss because of the attenuation effects. Moreover, note that the waveform distortion of the second reflection and the last reflection is more severe for the lower water saturations (Fig. 29(b)) while the most severe waveform distortion appeared in a specific saturation ratio in the case of 1:3 oil-gas proportion (Fig. 30(b)). In Fig. 30(b), the waveform distortion of the second and third reflections is more severe when $S_w = 0.5$ compared with the two cases of $S_w = 0$ and $S_{\rm w} = 1$, demonstrating that the dispersion and attenuation are the most severe in this situation. For the case of 3:1 oil-gas proportion and water saturated rock, the seismic records shown in Fig. 31(a) illustrate that the reflection features are very similar to the Fig. 29(a). However, the waveform distortion of the seismic reflections is more severe than the previous two cases for a lower water saturation (Fig. 31(b)), which indicates that the velocity dispersion is more severe in the frequency band of seismic exploration when the rock is saturated with three-phase immiscible fluids in the case of higher oil saturation and lower water saturation. The numerical modeling of the seismic responses demonstrates that the velocity dispersion and attenuation within the frequency band of seismic exploration can lead to more severe waveform distortion when the oil content increases. The results are consistent with the phenomenon that strong dispersion can be observed in a lower frequency band as shown in Fig. 27(b).

3.4.2. Real seismic data analysis

To verify the accuracy of the results of numerical analysis, we use the log data and real field seismic data to further provide the evidence of our work. Firstly, we analysed the frequency-dependent velocities and attenuations of fluid-saturated reservoirs with different gas saturation based on the real log curves. Fig. 32(a) shows the well-logs through the sandstone reservoir, including water saturation ($S_{\rm w}$), P-wave, S-wave and density curves. The color rectangles outline the fluid-saturated reservoirs saturated with different gas saturation (high gas-saturated zone with the $S_{\rm g}=0.6$, low gas-saturated zone with the $S_{\rm g}=0.3$ and water-saturated zone with the $S_{\rm g}=0.3$ and $S_{$



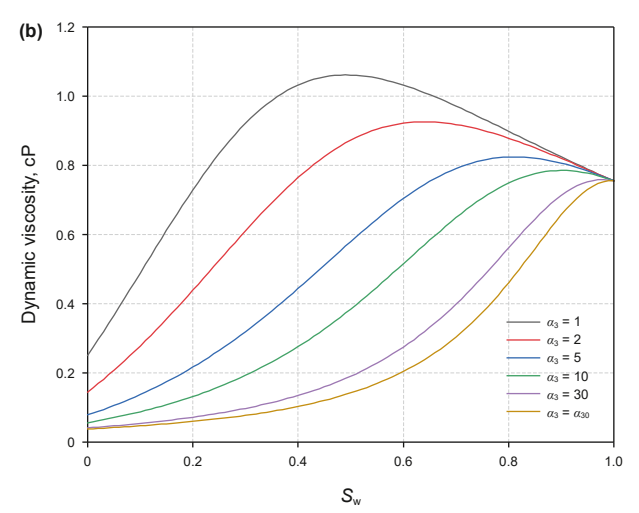


Fig. 19. The effective fluid modulus (a) and fluid viscosity (b) when α_3 given six different values and $\alpha_2 = 1$ for three-phase immiscible fluids and the ratio of the oil and gas is 1:3.

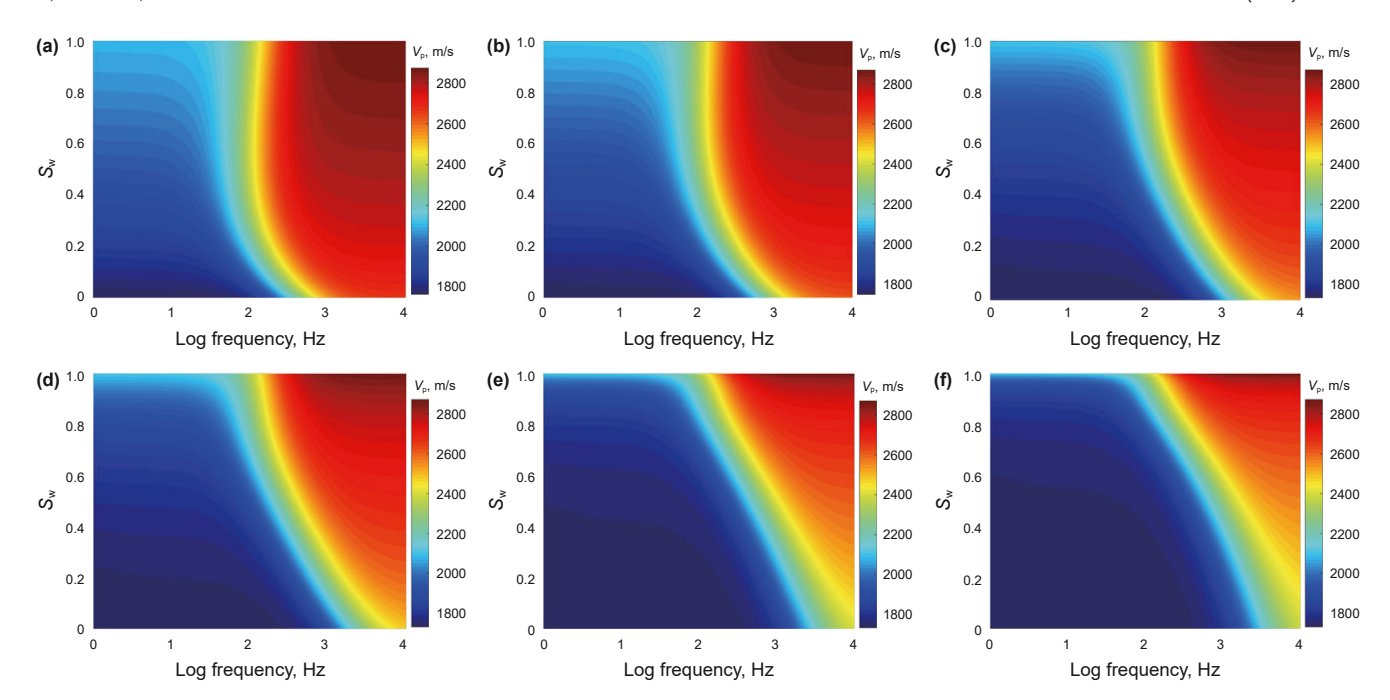


Fig. 20. The distributions of frequency-dependent velocity of P-wave on the frequency and water saturation plane when α_3 given six different values and $\alpha_2 = 1$ for the rock saturated with water, oil and gas and the ratio of the oil and gas is 1:3. (a) $\alpha_3 = 1$; (b) $\alpha_3 = 2$; (c) $\alpha_3 = 5$; (d) $\alpha_3 = 10$; (e) $\alpha_3 = 30$; (f) $\alpha_3 = \alpha_{30}$.

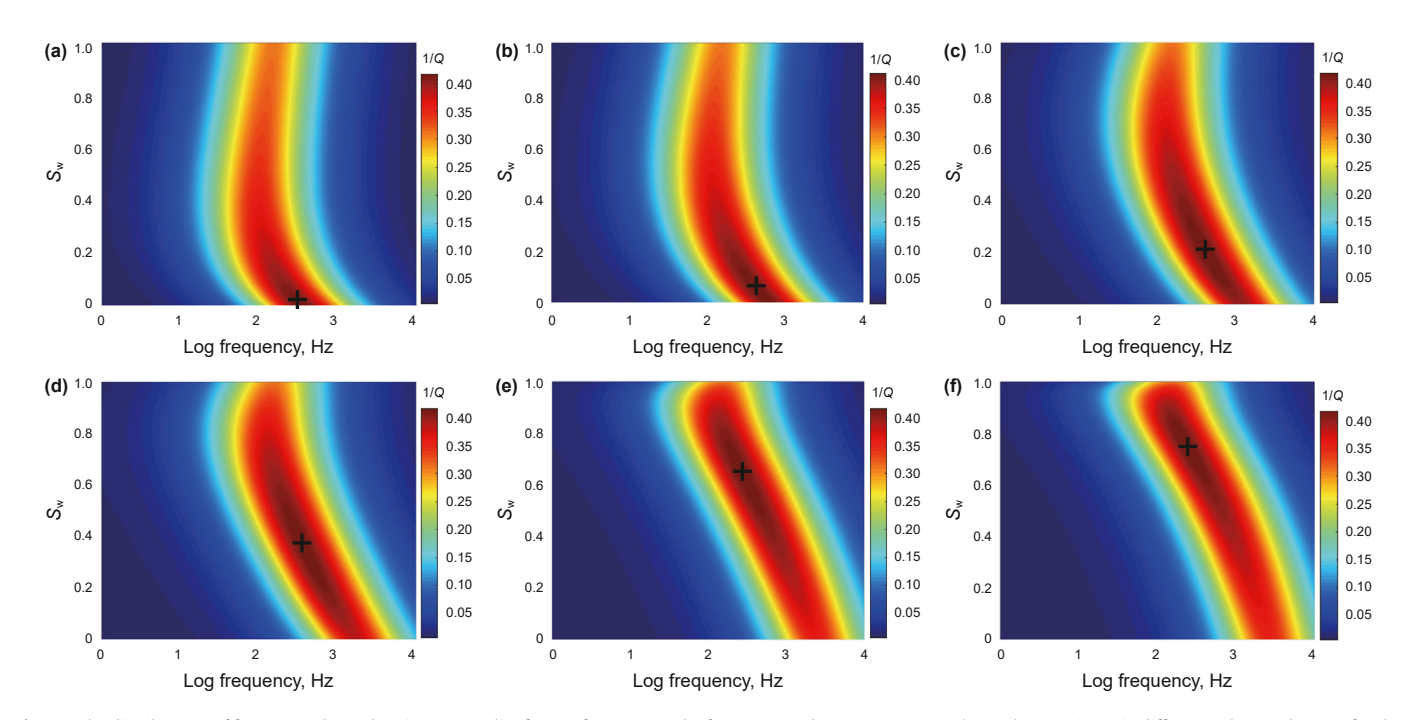


Fig. 21. The distributions of frequency-dependent inverse quality factor of P-wave on the frequency and water saturation plane when α_3 given six different values and $\alpha_2 = 1$ for the rock saturated with water, oil and gas and the ratio of the oil and gas is 1:3. (a) $\alpha_3 = 1$; (b) $\alpha_3 = 2$; (c) $\alpha_3 = 5$; (d) $\alpha_3 = 10$; (e) $\alpha_3 = 30$; (f) $\alpha_3 = \alpha_{30}$.

second column) and density curves (in the fourth column) show a change to lower values, corresponding to the elastic zone. Fig. 32(b) shows the real seismic angle gathers at the location of the well and its stacked trace (Fig. 32(c)).

Then, we calculate the frequency-dependent velocities and attenuations of the hydrocarbon reservoirs saturated with different gas saturations using the proposed method. The parameters (Table 4) of fluid-saturated reservoirs used in the calculations are given by the real log data. The porosity of porous medium is 18%

given from the real log data and other parameters of the reservoir rock are referenced the values of Table 1. The basic properties of gas and water used in numerical modeling are referenced the values of Table 2. The results of the frequency-dependent velocities shown in Fig. 33 illustrates that the velocity moves toward higher value with decreasing gas saturation. However, the velocities when gas saturations are 0.6, 0.3 are decreased in the seismic frequency band for α_3 increasing. The main reason is that the characteristic frequency shifts to a higher frequency as the α_3 increases.

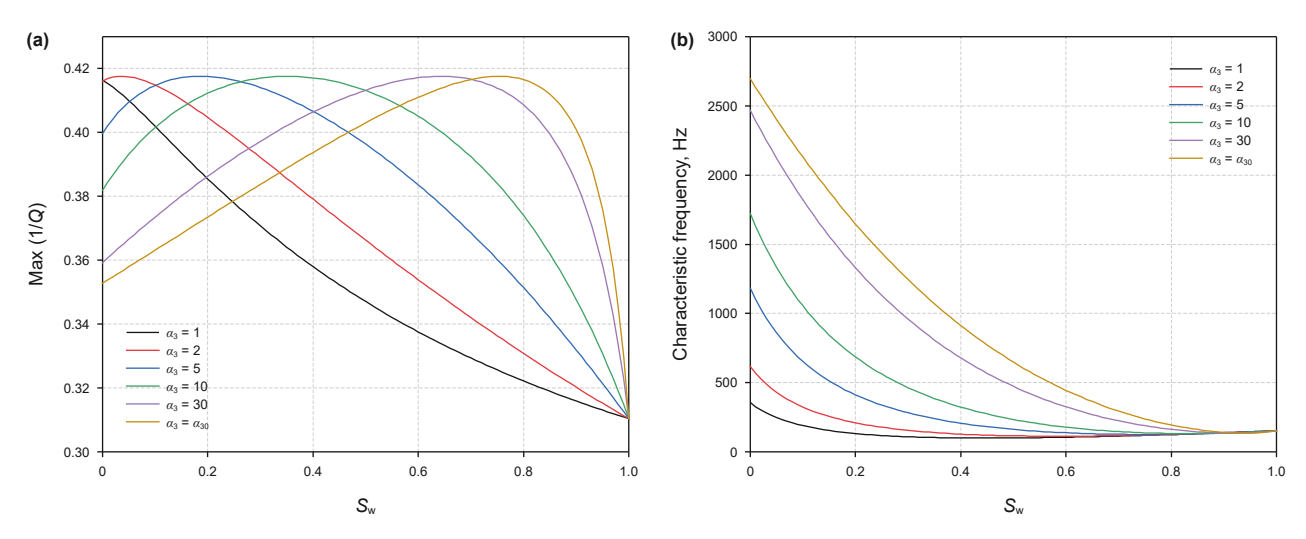


Fig. 22. (a) Attenuation peaks and (b) characteristic frequencies when α_3 given six different values and $\alpha_2 = 1$ for the rock saturated with water, oil and gas and the ratio of the oil and gas is 1:3.

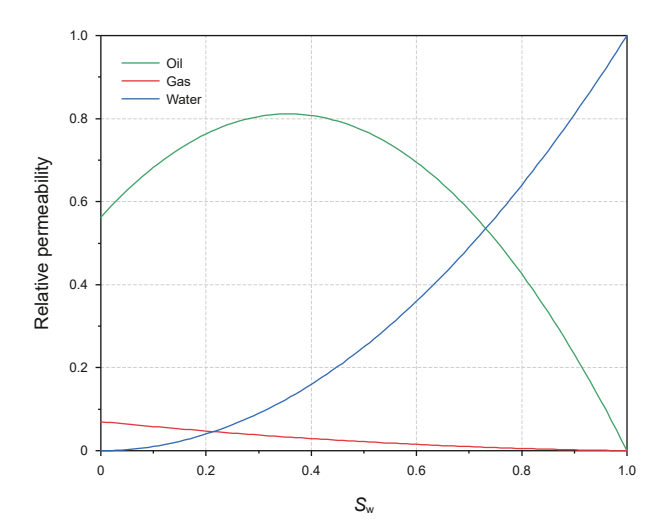


Fig. 23. Relative permeabilities for the rock saturated with water, oil and gas and the ratio of the oil and gas is 3:1.

Next, based on the calculated frequency-dependent velocities, we use the phase-shift method (Chen et al., 2016b) in the frequency wavenumber domain to generate the seismic angle gathers. The synthetic seismic records were generated by using a Ricker wavelet with the dominant frequency of 35 Hz. Here, we compared the synthetic seismic angles with the real seismic angle gathers and calculated the correlation coefficient between the two data sets. When conducting the synthetic seismic angle gathers, the velocities of the three types reservoirs with different saturation are frequency-dependent (as shown in the Fig. 33), which are calculated based on the data in Table 4 under different capillary parameters. Besides, rather than parameters at the reservoir location using the data from the well in Fig. 32. Then, the seismic stacked traces can be generated when α_3 given different values. Fig. 34 shows the comparison results between the stacked trace of real seismic angle gathers with the staked trace of synthetic seismic angle gathers when α_3 given different values. As shown in Fig. 34, the waveform, amplitude, and travel time of the synthetic seismic trace is matched well with the real seismic trace when $\alpha_3 = 1$. However, as α_3 increases, the similarity of the waveform decreases

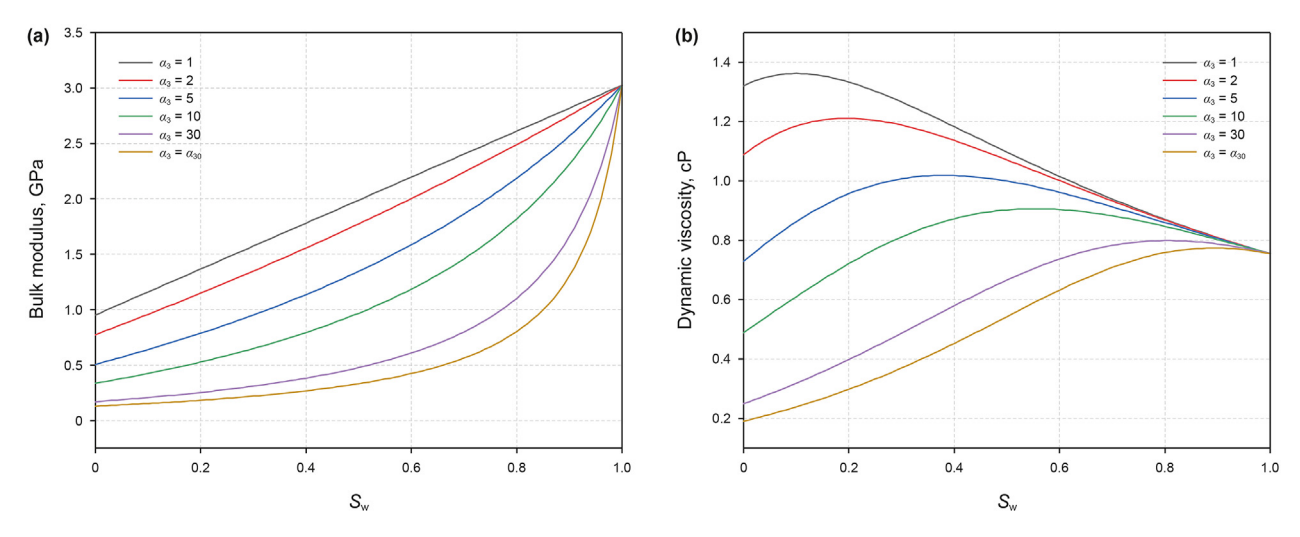


Fig. 24. The effective fluid modulus (a) and fluid viscosity (b) when α_3 given six different values and $\alpha_2 = 1$ for three-phase immiscible fluids and the ratio of the oil and gas is 3:1.

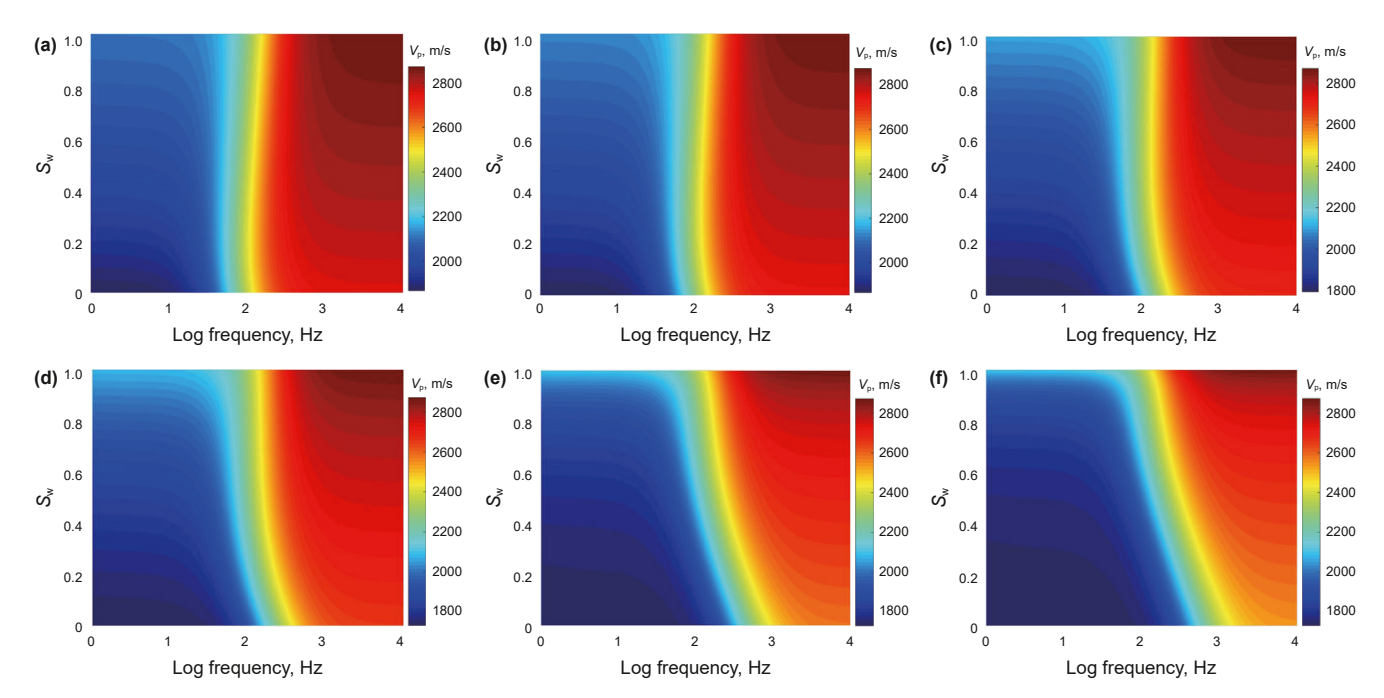


Fig. 25. The distributions of frequency-dependent velocity of P-wave on the frequency and water saturation plane when α_3 given six different values and $\alpha_2 = 1$ for the rock saturated with water, oil and gas and the ratio of the oil and gas is 3:1. (a) $\alpha_3 = 1$; (b) $\alpha_3 = 2$; (c) $\alpha_3 = 5$; (d) $\alpha_3 = 10$; (e) $\alpha_3 = 30$; (f) $\alpha_3 = \alpha_{30}$.

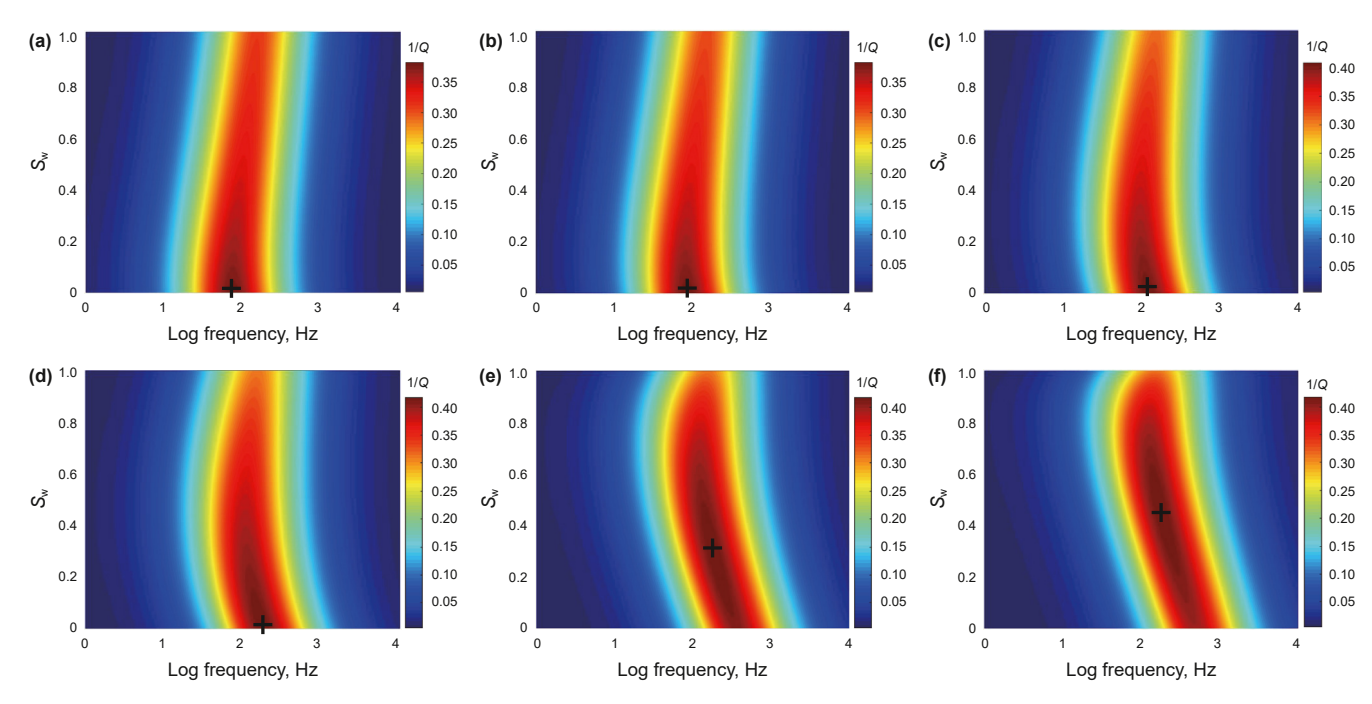


Fig. 26. The distributions of frequency-dependent inverse quality factor of P-wave on the frequency and water saturation plane when α_3 given six different values and $\alpha_2 = 1$ for the rock saturated with water, oil and gas and the ratio of the oil and gas is 3:1. (a) $\alpha_3 = 1$; (b) $\alpha_3 = 2$; (c) $\alpha_3 = 5$; (d) $\alpha_3 = 10$; (e) $\alpha_3 = 30$; (f) $\alpha_3 = \alpha_{30}$.

and the amplitude difference of seismic reflections in the reservoir zone becomes bigger. Besides, the deviation of the reflection time at reservoir interface also becomes larger. The main reason is that the strong velocity dispersion occurred in the seismic frequency band for a lower α_3 , which is consistent with the conclusion of our numerical analysis. When the α_3 increases, the characteristic frequency moves towards to a higher frequency, resulting in lower velocities remaining within the seismic frequency band, which in turn affects the arrival time and energy changes of seismic

reflections. The correlation coefficients between the stacked trace of real seismic angle gathers with the stacked trace of synthetic seismic angle gathers for different α_3 are shown in Fig. 35. The results also indicates that the correlation coefficient is maximum when $\alpha_3=1$, and decreases with the increase of α_3 . To further explain the phenomenon in Fig. 34, four reflection positions (A, B, C, D) from Fig. 34 were selected, and their arrival times and reflection amplitudes were quantitatively compared in Fig. 36. As shown in Fig. 36(a), when $\alpha_3=1$, the arrival times at the four reflection



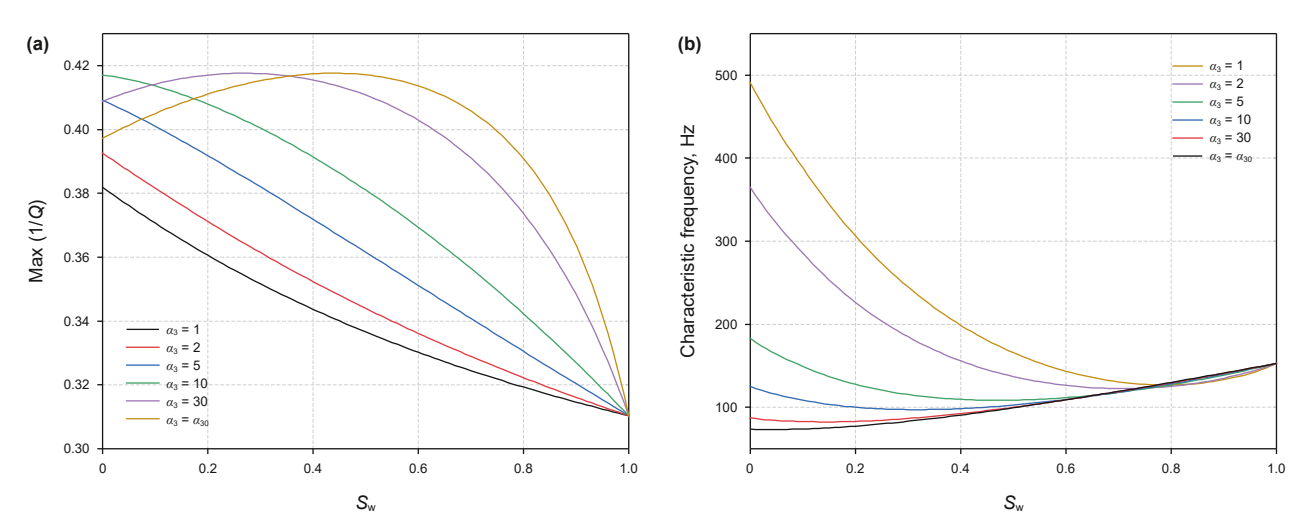


Fig. 27. (a) Attenuation peaks and **(b)** characteristic frequencies when α_3 given six different values and $\alpha_2 = 1$ for the rock saturated with water, oil and gas and the ratio of the oil and gas is 3:1.

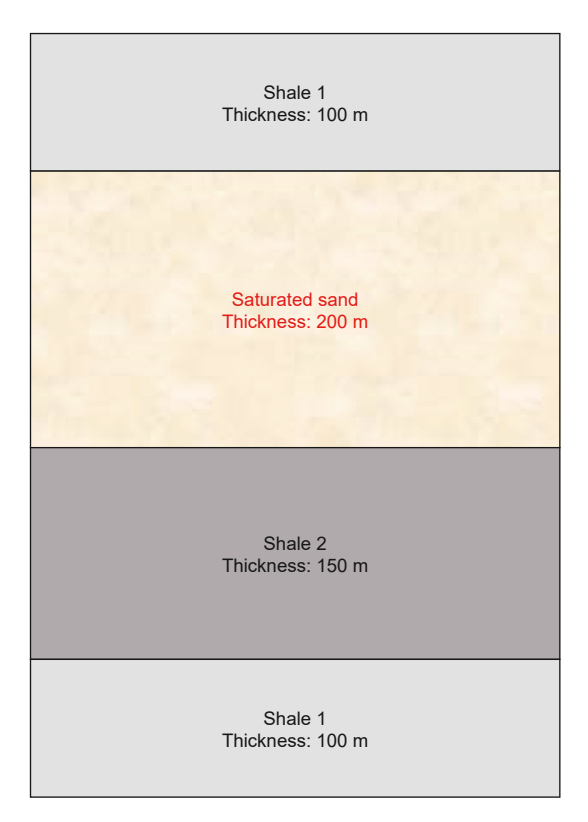


Fig. 28. The fluid-saturated model with four layers used to produce seismic records.

positions are closest to those in the original seismic record. Therefore, the capillary parameter plays an essential role for controlling the characteristics of the velocity which should not be neglected when analyse the frequency-dependent seismic responses.

Table 3The parameters of the shales used in the seismic modeling.

Properties	Shale 1	Shale 2
$V_{\rm p}$, m/s	2755	2975
$V_{\rm s}$, m/s	1402	1595
ρ , kg/m ³	2070	2200

Finally, we use the seismic angle gathers synthetized by the Zoeppritz equation and our method to compare with the real seismic angle gathers. The results shown in Fig. 37 indicates that the reflection features of the seismic angle gathers synthetized by the Zoeppritz equation in Fig. 37(b) don not match well with the real seismic angle gathers (Fig. 37(a)). The reflection times at the bottom reservoir interfaces (bule line and the bottom red line) exhibits time delay compared with the Fig. 37(a) and the reflection amplitudes above the reservoirs are very weak. However, when considering the influence of relative permeability, capillary parameter, and reservoir wettability on the velocity dispersion, the seismic angle gathers in Fig. 37(c) generated by the diffusiveviscous wave equation show excellent similarity with real seismic angle gathers shown in Fig. 37(a), in respect of seismic amplitude, waveform, and travel time. The correlation coefficient between the stacked trace in Fig. 37(a) and the stacked trace synthesized using the Zoeppritz equation in Fig. 37 (b) is 0.7234, which is lower than the correlation coefficient shown in Fig. 35 when $\alpha_3 = 1$. Thus, the synthetic seismic angle gathers, considering velocity dispersion and a suitable capillary parameter, exhibit better consistency with real seismic data, demonstrating the potential of these methodologies for practical reservoir characterization.

4. Discussion

This study investigates the seismic response of porous rocks saturated with three-phase immiscible fluids, a topic that has been less explored in the context of multiphase flow for geophysical applications. To emphasize the importance of relative permeability and capillary pressure in the dispersion and attenuation of porous rocks saturated with three-phase immiscible fluids, we employ the relative permeability equation proposed by Bianchi Janetti et al. (2016), which incorporates the viscosity ratio, and introduce capillary pressure through a derivation by Papageorgiou et al. (2016) to delineate the dispersive effects. However, the relative permeability model used in the study assumes that the three-phase flow conditions are restricted to perfectly water-wet systems, where water coats the pore walls, gas occupies the pore centers, and oil acts as an intermediate-wettability phase. This simplifies the fluid distribution but may not reflect real-world reservoirs with mixed or variable wettability. Meanwhile, the parameters α_2 and α_3 , which link fluid pressures via capillary effects, are treated as free variables lacking rigorous physical justification or empirical validation, necessitating experimental verification the results of our

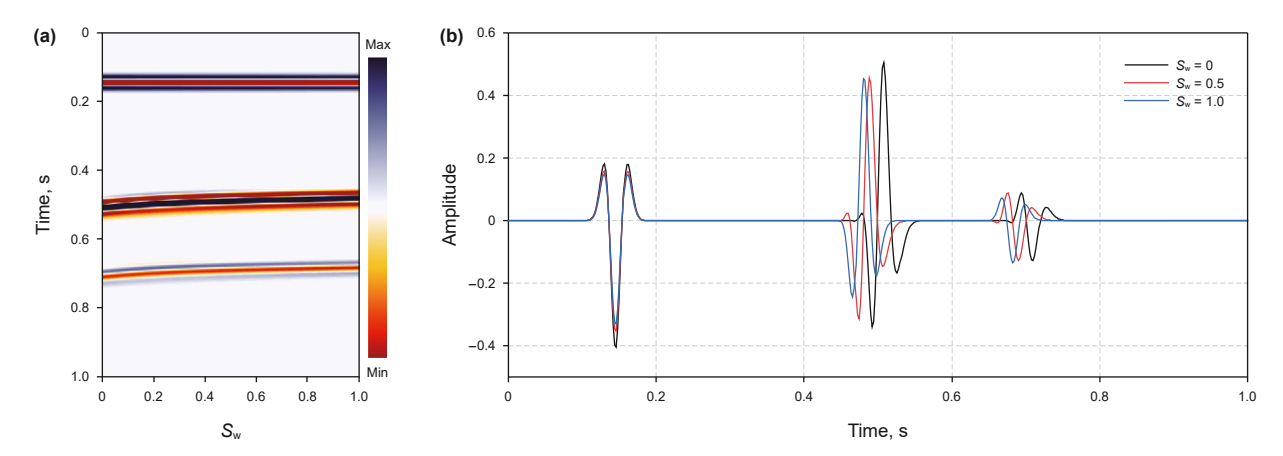


Fig. 29. (a) Seismic records of the designed model when S_w changes from 0 to 1 (for the case of the sand rock saturated with three-phase immiscible fluids with the proportion of oil and gas is 1:1) and (b) seismic traces extracted at three specific water saturations from Fig. 29 (a).

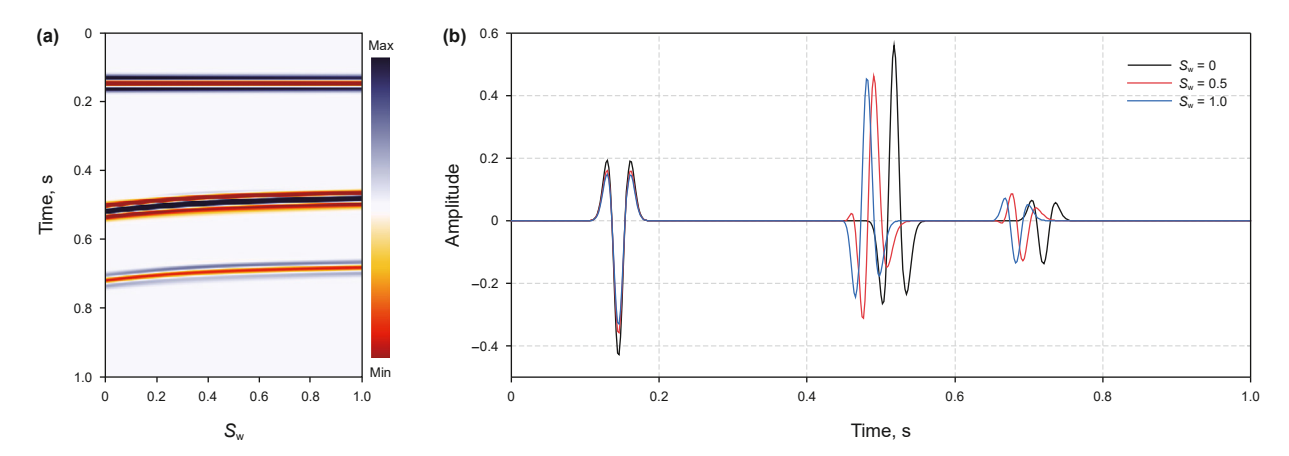


Fig. 30. (a) Seismic records of the designed model when S_w changes from 0 to 1 (for the case of the sand rock saturated with three-phase immiscible fluids with the proportion of oil and gas is 1:3) and (b) seismic traces extracted at three specific water saturations from Fig. 30 (a).

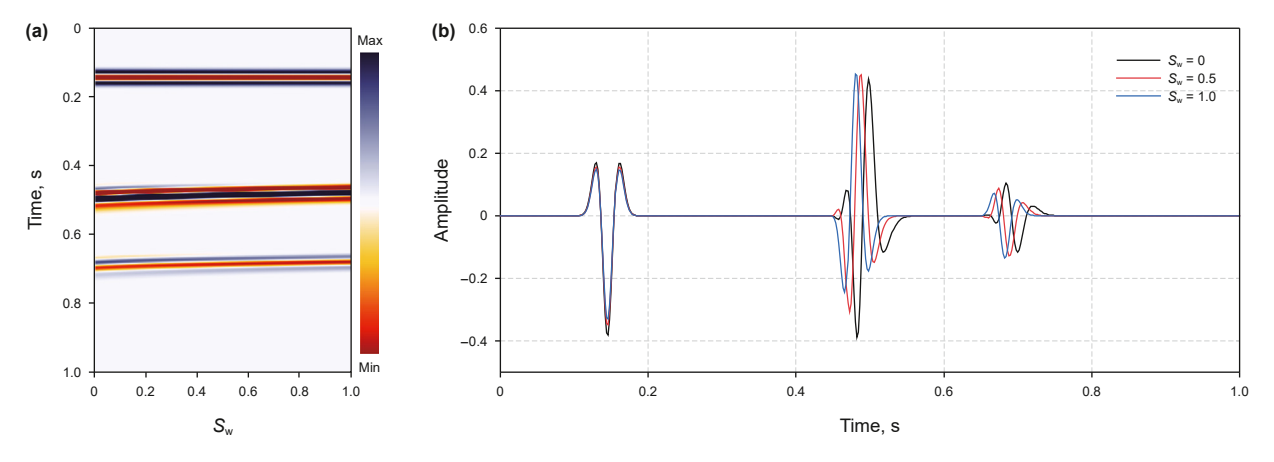


Fig. 31. (a) Seismic records of the designed model when S_w changes from 0 to 1 (for the case of the sand rock saturated with three-phase immiscible fluids with the proportion of oil and gas is 3:1) and (b) seismic traces extracted at three specific water saturations from Fig. 31(a).

method. Besides, the study extends two-phase models to three-phase systems but does not fully account for interactions like oilgas-water interfacial tension or phase trapping, which are also critical in real multiphase flow. Therefore, the complexity of multiphase fluid interactions warrants further investigation of

frequency-dependent velocity and attenuation of rocks saturated with three-phase immiscible fluids.

In the study, we propose a new calculation formula of effective fluid modulus when porous rock saturated with three-phase immiscible fluids. The Eq. (9) indicates that the effective fluid

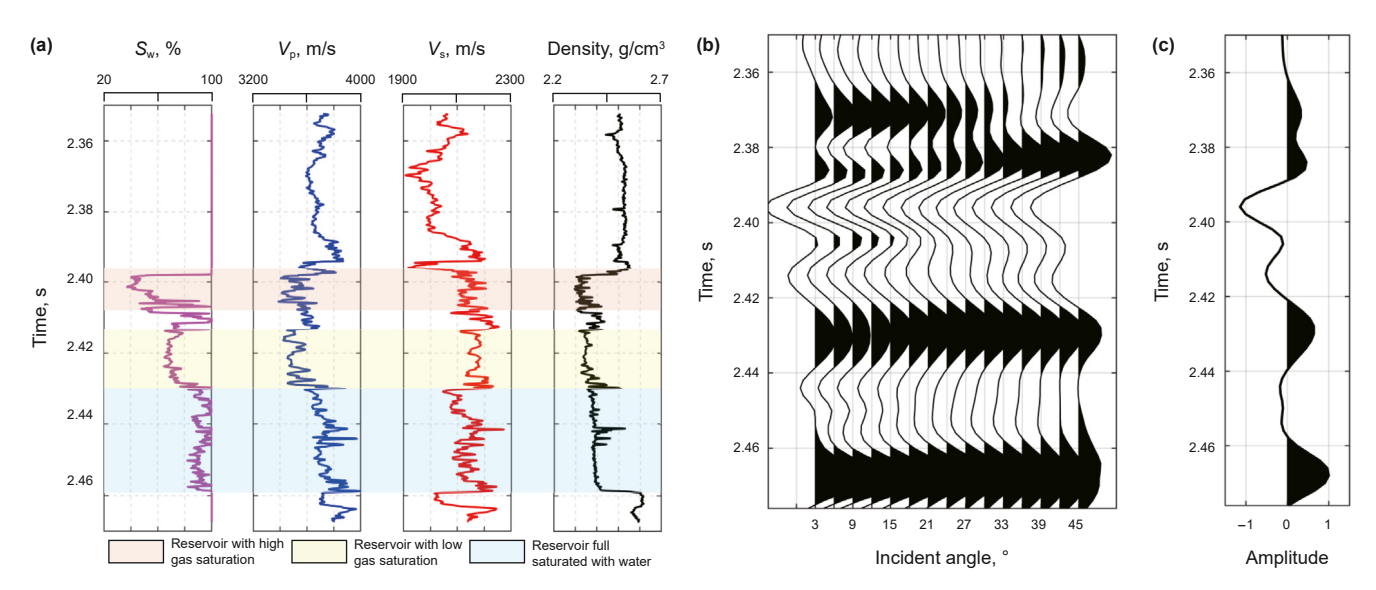


Fig. 32. (a) Well log curves of the sandstone reservoir; (b) seismic angle gathers at the location of the well and (c) stacked trace of all angles.

Table 4The parameters of fluid-saturated reservoirs used in the calculations.

Properties	Reservoir with high gas saturation	Reservoir with low gas saturation	Reservoir full saturated with water
V _p , m/s	3465	3500	3700
$V_{\rm s}$, m/s	2147	2165	2135
$S_{ m g}$	0.6	0.3	0

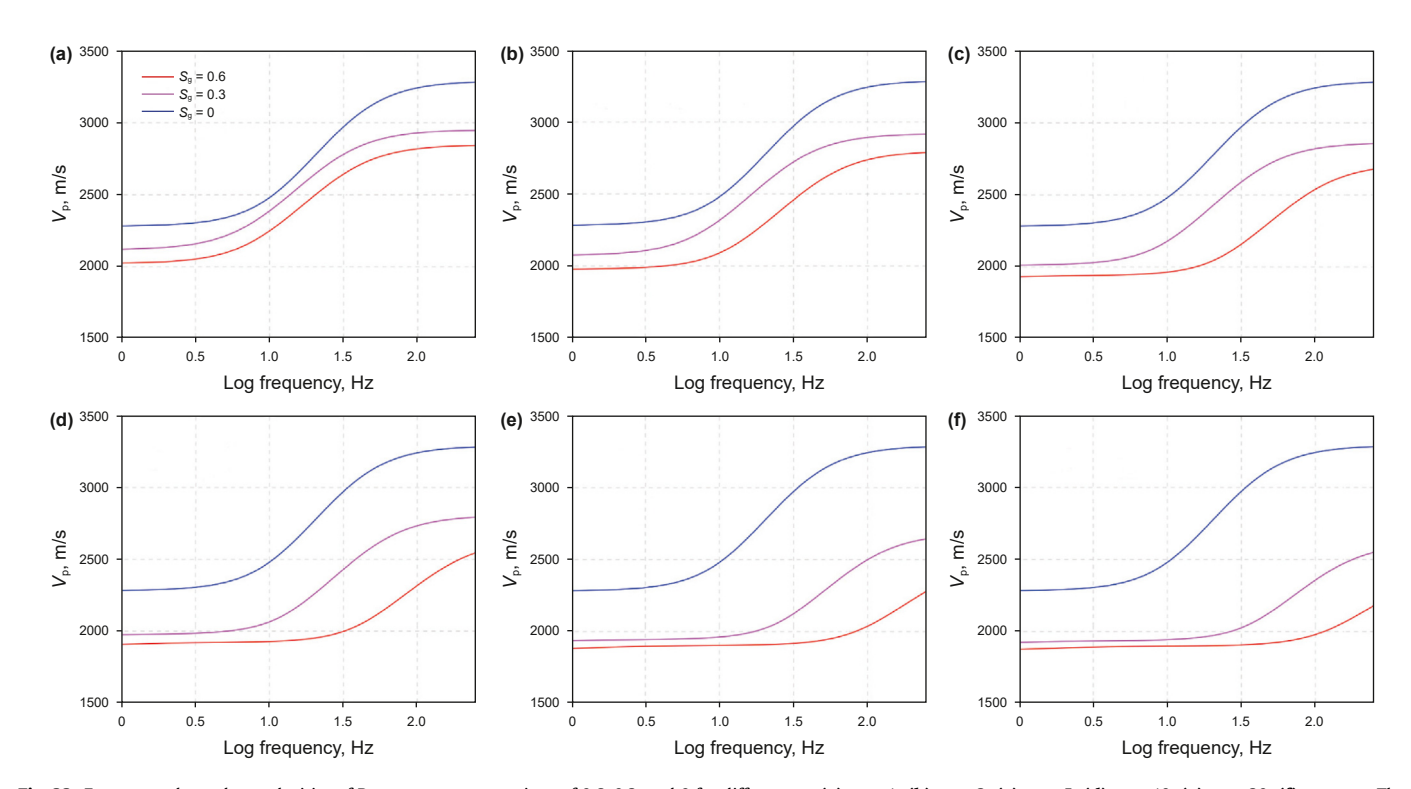


Fig. 33. Frequency-dependent velocities of P-wave at gas saturations of 0.6, 0.3, and 0 for different α_3 . (a) $\alpha_3 = 1$; (b) $\alpha_3 = 2$; (c) $\alpha_3 = 5$; (d) $\alpha_3 = 10$; (e) $\alpha_3 = 30$; (f) $\alpha_3 = \alpha_{30}$. The results are calculated using the values given by the real log data.

modulus is affected by the two free parameters α_2 and α_3 that are associated with the capillary pressure. However, the numerical results indicate that the effective fluid modulus show a small

difference due to the small variation range of α_2 when α_3 is fixed (Figs. 4 and 5) while show a significant variation for α_3 changes when α_2 is fixed (Figs. 2 and 3). This phenomenon reveals that the

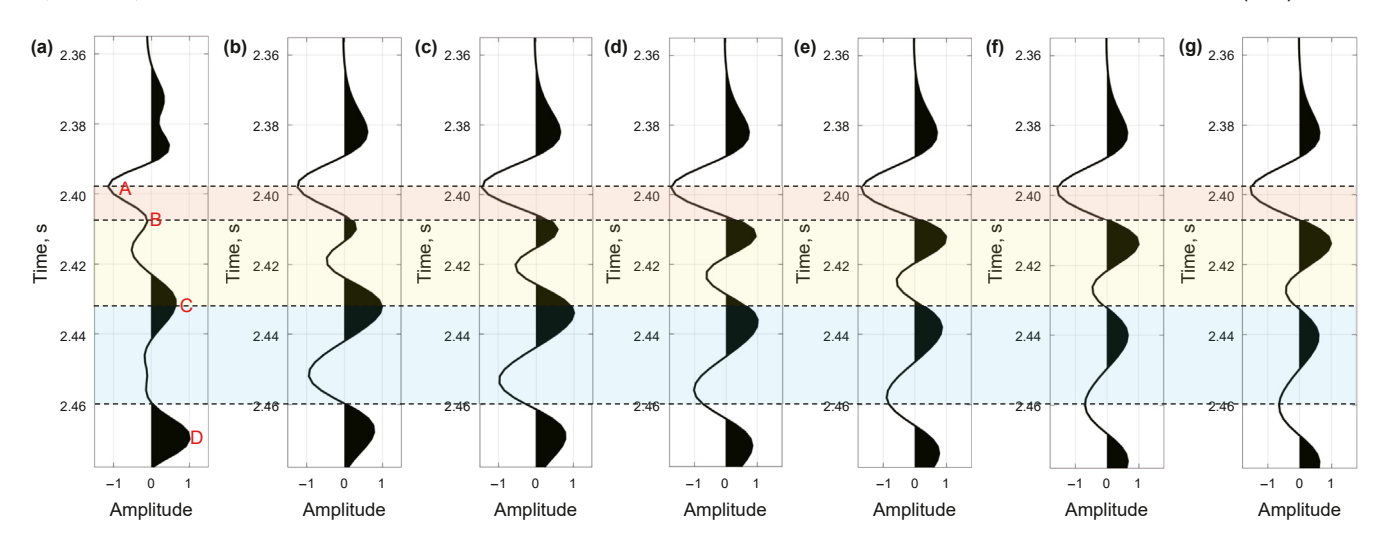


Fig. 34. The comparison between the stacked trace of real seismic angle gathers with the staked trace of all angles when α_3 given different values. (a) The staked trace of real seismic angle gathers and the stacked trace of synthetic angle gathers for α_3 given different values: (b) $\alpha_3 = 1$; (c) $\alpha_3 = 2$; (d) $\alpha_3 = 5$; (e) $\alpha_3 = 10$; (f) $\alpha_3 = 30$; (g) $\alpha_3 = \alpha_{30}$.

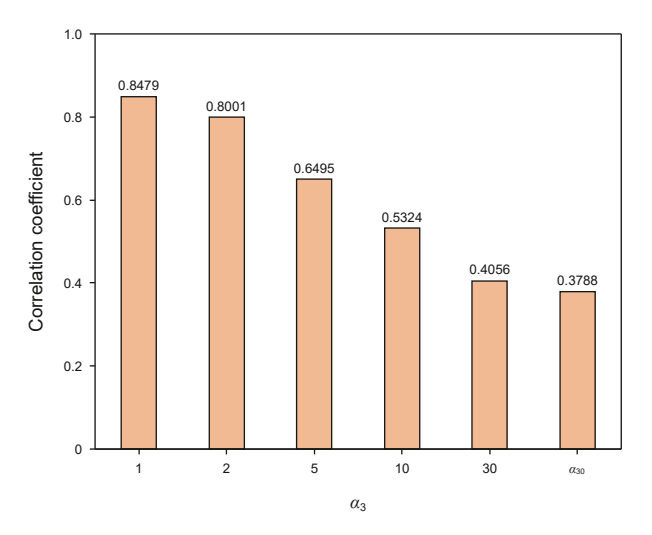


Fig. 35. The correlation coefficients between the stacked trace of real seismic angle gathers with the stacked trace of synthetic seismic angle gathers for different α_3 .

significant difference in physical properties between water and gas is more likely to cause changes in the modulus, which further increases the distinguishability between the two fluids. However, compared to water and gas, the smaller difference in physical properties between water and oil leads to a smaller difference in modulus, which may pose some difficulty in distinguishing between water and oil. These results may also provide a basis for fluid identification.

Moreover, the numerical results demonstrate that the dispersion and attenuation of seismic waves are significantly influenced by key factors such as capillary pressure, fluid proportions, and relative permeability. The fluid proportions and fluid pressures of multiphase mixed fluids in porous media can lead to considerable changes in the characteristic frequency and attenuation peak. For a lower α_3 , strong dispersive phenomena may occur in a lower frequency range. Besides, the relative permeability strongly depends on the fluid viscosity ratio which plays an essential role in controlling the relaxation time and will influences the frequency band of dispersive behavior that occurs. The main reason for this is that the effective fluid viscosity is greatly affected by the relative permeability according to the Eq. (12).

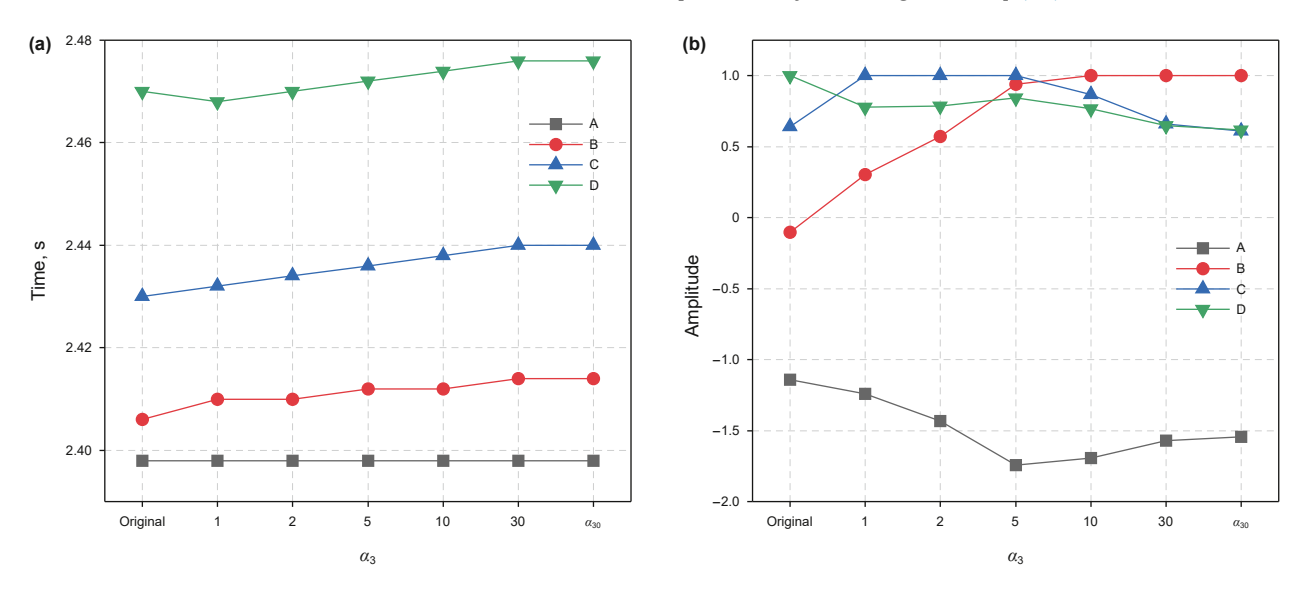


Fig. 36. The quantitative comparison of (a) the arrival time and (b) amplitude energy when α_3 changes at the four locations in Fig. 34.

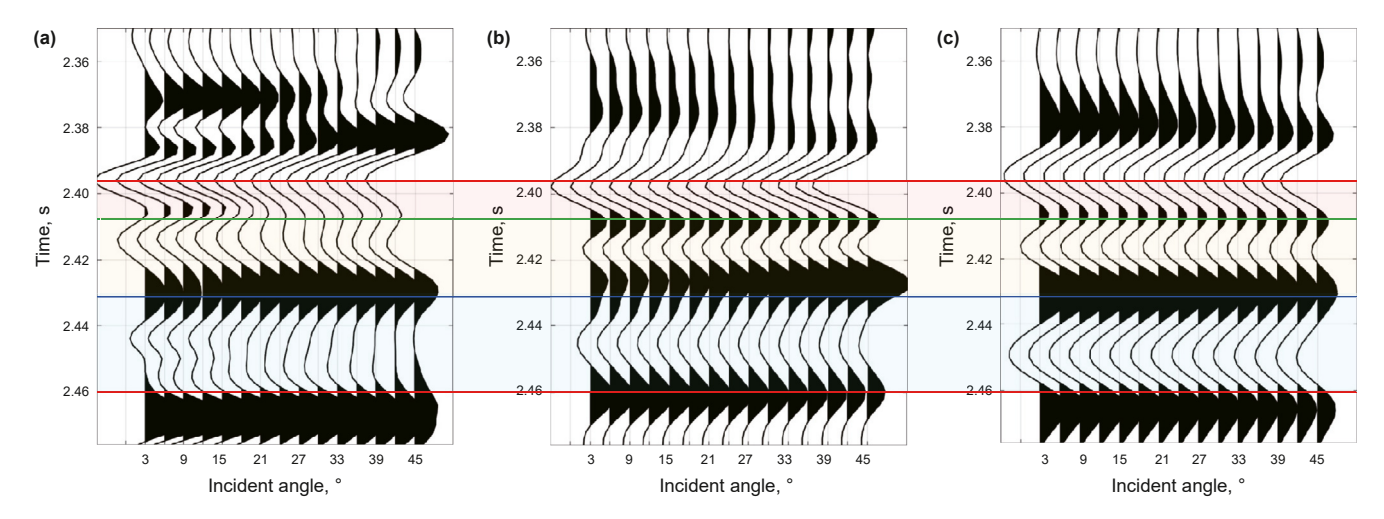


Fig. 37. (a) The real seismic angle gathers and seismic angle gathers calculated by (b) the Zoeppritz equation and (c) our method.

The fluid proportions, particularly the oil content, also contribute substantially to these behaviors, indicating that variations in fluid phase distribution within the rock matrix could significantly alter the seismic responses. This phenomenon further supports the findings of previous studies (Batzle et al., 2006; Chen et al., 2016a; Luo et al., 2022), suggesting that the velocity dispersion and attenuation resulting from wave-induced flow of viscous fluids in porous rocks within the seismic frequency range are influenced by the wetting phase. Thus, considering these factors comprehensively can better explain the dispersion and attenuation phenomena within the seismic frequency band.

In addition, the study reveals that the reflection characteristics, such as travel time, seismic amplitude, and waveform, are sensitive to both the fluid proportions and capillary pressure. As shown in Fig. 35, the correlation coefficients between the stacked trace of real seismic angle gathers with the stacked trace of synthetic seismic angle gathers show the best correlation when $\alpha_3=1$. The results indicate that we can ignore the effects of the parameter α_3 and only adjust the parameters α_1 and α_2 when use this method to synthetic a reasonable seismic trace for a porous rock saturated with three-phase immiscible fluids. These findings suggest that seismic techniques could be employed as a viable tool for assessing the distribution of multiphase fluids in subsurface reservoirs. Moreover, the validation using real seismic data confirms the relevance of our theoretical model to actual geological settings, demonstrating the potential for these methodologies in practical reservoir characterization.

While validated numerically and against limited field data, the proposed models lack rigorous experimental verification (e.g., lab measurements of three-phase dispersion/attenuation). However, due to the consideration of multiple factors affecting velocity dispersion and attenuation in this study, the experimental conditions are difficult to meet the research needs. Therefore, more laboratory and field data should be further test to validate the accuracy of the results in the future.

5. Conclusions

We propose the calculation formulas of effective fluid modulus and effective fluid viscosity when the relative permeability, capillary parameter, and reservoir wettability are considered simultaneously. The method is suitable for the case of the combined saturation for any fluid type and provides theoretical support to explore the behaviors caused by WIFF when a porous rock saturated with multiphase immiscible fluids.

By incorporating factors such as capillary pressure, relative permeability, and fluid proportions, we have developed a comprehensive model for analyzing the frequency-dependent behaviors of such systems. The results show that seismic dispersion and attenuation are significantly influenced by these factors, with lower capillary pressure parameter α_3 and higher oil content leading to more pronounced seismic effects. Furthermore, the study highlights that the seismic reflection characteristics (amplitude, waveform distortion, and travel time) of a porous rock saturated with three-phase immiscible fluids are obviously influenced by fluid proportions and capillary parameter. Notably, more severe waveform distortion can be observed within the seismic exploration frequency band when the rock is saturated with three-phase immiscible fluids in the case of higher oil saturation and lower water saturation for a lower α_3 .

The synthetic seismic angle gathers considering the velocity dispersion exhibit better consistency with real seismic data when appropriate capillary parameters are applied. The numerical modeling method, which considers the relative permeability, capillary parameter, and reservoir wettability can provide more reasonable seismic angle gathers associated with the dispersion effects for the frequency-dependent AVO analysis. It is significant to further guide the extraction of dispersion anomalies associated with the porous rock within the seismic frequency range from real seismic data by employing the frequency-dependent AVO inversion.

Despite the fact that this study concentrates on numerical modeling, the results provide an important implication for deeper understanding the WIFF-caused dispersion and attenuation mechanism in multiphase immiscible fluid-saturated rocks. This numerical modeling results reveal that the contributions of the relative permeability, capillary parameters, and reservoir wettability to the dispersion and attenuation of multiphase fluids should not be neglected. The method is particularly suited for reservoirs characterized by porous rocks saturated with multiphase immiscible fluids, making it relevant for hydrocarbon exploration and production, as well as other industrial processes involving such reservoirs.

CRediT authorship contribution statement

Xin Luo: Writing — original draft, Methodology, Formal analysis, Conceptualization. **Xue-Hua Chen:** Writing — review & editing, Resources, Conceptualization. **Tong Li:** Visualization. **Gui-Rong Luo:** Visualization, Software. **Peng Wang:** Writing — review & editing.

Data availability

The data are available from the corresponding author upon reasonable request.

Declaration of competing interest

The authors declare that they have no known competing financial interests or personal relationships that could have appeared to influence the work reported in this paper.

Acknowledgements

This work is supported in part by the National Natural Science Foundation of China under Grant 41874143 and Grant 42374163, and in part by the Key Program of Natural Science Foundation of Sichuan Province of China under Grant 2023NSFSC0019, and in part by the Central Funds Guiding the Local Science and Technology Development under Grant 2024ZYD0124.

References

- Ahmad, Q.A., Wu, G., Zong, Z., Wu, J., Li, K., Du, T., Khan, N., 2020. Analysis of attenuation and dispersion of propagating wave due to the coexistence of three fluid phases in the pore volume. Geophys. Prospect. 68, 657–677. https://doi.org/10.1111/1365-2478.12873.
- Alkhimenkov, Y., Caspari, E., Gurevich, B., Barbosa, N.D., Glubokovskikh, S., Hunziker, J., Quintal, B., 2020. Frequency-dependent attenuation and dispersion caused by squirt flow: three-dimensional numerical study. Geophysics 85, MR129—MR145. https://doi.org/10.1190/geo2019-0519.1.
- Arntsen, B., Carcione, J.M., 2001. Numerical simulation of the Biot slow wave in water-saturated Nivelsteiner Sandstone. Geophysics 66, 890–896. https://doi.org/10.1190/1.1444978.
- Batzle, M.L., Han, D.H., Hofmann, R., 2006. Fluid mobility and frequency-dependent seismic velocity - direct measurements. Geophysics 71, 1–9. https://doi.org/ 10.1190/1.2159053.
- Batzle, M., Wang, Z.J., 1992. Seismic properties of pore fluids. Geophysics 57, 1396–1408. https://doi.org/10.1190/1.1443207.
- Bianchi Janetti, E., Riva, M., Guadagnini, A., 2016. Analytical expressions for three-phase generalized relative permeabilities in water- and oil-wet capillary tubes. Comput. Geosci. 20, 555–565. https://doi.org/10.1007/s10596-015-9508-5.
- Biot, M.A., 1956a. Theory of propagation of elastic waves in a fluid-saturated porous solid. I. Low-frequency range. J. Acoust. Soc. Am. 28, 168–178. https://doi.org/10.1121/1.1908239.
- Biot, M.A., 1956b. Theory of propagation of elastic waves in a fluid-saturated porous solid. II. Higher-frequency range. J. Acoust. Soc. Am. 28, 179–191. https:// doi.org/10.1121/1.1908241.
- Borgomano, J.V.M., Pimienta, L.X., Fortin, J., Guéguen, Y., 2019. Seismic dispersion and attenuation in fluid-saturated carbonate rocks: effect of microstructure and pressure. J. Geophys. Res. Solid Earth 124, 12498–12522. https://doi.org/ 10.1029/2019|B018434.
- Brajanovski, M., Gurevich, B., Schoenberg, M., 2005. A model for P-wave attenuation and dispersion in a porous medium permeated by aligned fractures. Geophys. J. Int. 163, 372–384. https://doi.org/10.1111/j.1365-246X.2005.02722.x.
- Carcione, J.M., Picotti, S., 2006. P-wave seismic attenuation by slow-wave diffusion: effects of inhomogeneous rock properties. Geophysics 71, O1–O8. https://doi.org/10.1190/1.2194512.
- Caspari, E., Qi, Q.M., Lopes, S., Lebedev, M., Gurevich, B., Rubino, J.G., Velis, D.R., Clennell, M.B., Müller, T.M., 2014. Wave attenuation in partially saturated porous rocks-New observations and interpretations across scales. Lead. Edge 33, 606–614. https://doi.org/10.1190/tle33060606.1.
- Chapman, M., Maultzsch, S., Liu, E., Li, X., 2003. The effect of fluid saturation in an anisotropic multi-scale equant porosity model. J. Appl. Geophys. 54, 191–202. https://doi.org/10.1016/j.jappgeo.2003.01.003.
 Chapman, M., Zatsepin, S.V., Crampin, S., 2002. Derivation of a microstructural
- Chapman, M., Zatsepin, S.V., Crampin, S., 2002. Derivation of a microstructural poroelastic model. Geophys. J. Int. 151, 427–451. https://doi.org/10.1046/j.1365-246X 2002 01769 x
- Chen, F., Zong, Z., Yin, X., 2022. Acoustothermoelasticity for joint effects of stress and thermal fields on wave dispersion and attenuation. J. Geophys. Res. Solid Earth 127, e2021JB023671. https://doi.org/10.1029/2021JB023671.
- Chen, F., Zong, Z., Yin, X., 2025. A squirt-flow model in isotropic porous rocks containing wedge-shaped cracks and its interpretation for laboratory measurements. Geophysics 90, MR141–MR153. https://doi.org/10.1190/geo2024-0282.1.
- Chen, F., Zong, Z., Yin, X., Yang, Z., Yan, X., 2023. Pressure and frequency dependence of elastic moduli of fluid-saturated dual-porosity rocks. Geophys. Prospect. 71, 1599—1615. https://doi.org/10.1111/1365-2478.13395.

Chen, X., Zhong, W., He, Z., Zou, W., 2016a. Frequency-dependent attenuation of compressional wave and seismic effects in porous reservoirs saturated with multi-phase fluids. J. Pet. Sci. Eng. 147, 371–380. https://doi.org/10.1016/ i.petrol.2016.08.031.

- Chen, X., Qi, Y., He, X., He, Z., Chen, H., 2016b. Phase-shifted based numerical method for modeling frequency-dependent effects on seismic reflections. Pure Appl. Geophys. 173, 2899–2912. https://doi.org/10.1007/s00024-016-1290-3.
- Chen, X., Zhong, W., Gao, G., Zou, W., He, Z., 2017. Numerical analysis of velocity dispersion in multi-phase fluid-saturated porous rocks. Pure Appl. Geophys. 174, 1219–1235. https://doi.org/10.1007/s00024-016-1457-y.
- Dupuy, B., Stovas, A., 2014. Influence of frequency and saturation on AVO attributes for patchy saturated rocks. Geophysics 79, B19–B36. https://doi.org/10.1190/geo2012-0518.1.
- Dutta, N.C., Ode, H., 1979a. Attenuation and dispersion of compressional waves in fluid-filled porous rocks with partial gas saturation (White model) - Part I: biot theory. Geophysics 44, 1777–1788. https://doi.org/10.1190/1.1440938.
- Dutta, N.C., Ode, H., 1979b. Attenuation and dispersion of compressional waves in fluid-filled porous rocks with partial gas saturation (White model) part II: results. Geophysics 44, 1789–1805. https://doi.org/10.1190/1.1440939.
- Dvorkin, J., Mavko, G., Nur, A., 1995. Squirt flow in fully saturated rocks. Geophysics 60, 97–107. https://doi.org/10.1190/1.1822622.
- Dvorkin, J., Nolen-hoeksema, R., Nur, A., 1994. The squirt-flow mechanism: macroscopic description. Geophysics 59, 428–438. https://doi.org/10.1190/
- Dvorkin, J., Nur, A., 1993. Dynamic porelasticity: a unified theory with the squirt and biot mechanisms. Geophysics 58, 524–533. https://doi.org/10.1190/1.1822168.
- Gallagher, A., Fortin, J., Borgomano, J., 2022. Seismic dispersion and attenuation in fractured fluid-saturated porous rocks: an experimental study with an analytic and computational comparison. Rock Mech. Rock Eng. 55, 4423–4440. https://doi.org/10.1007/s00603-022-02875-y.
- Guo, Z., Zhao, D., Liu, C., 2022. Gas prediction using an improved seismic dispersion attribute inversion for tight sandstone gas reservoirs in the Ordos Basin, China. J. Nat. Gas Sci. Eng. 101, 104499. https://doi.org/10.1016/j.jngse.2022.104499.
- Guo, Z., Zhao, T., Liu, C., 2023. Direct hydrocarbon identification in shale oil reservoirs using fluid dispersion attribute based on an extended frequency-dependent seismic inversion scheme. Pet. Sci. 20, 1532–1545. https://doi.org/10.1016/j.petsci.2022.12.011.
- Gurevich, B., Makarynska, D., de Paula, O.B., Pervukhina, M., 2010. A simple model for squirt-flow dispersion and attenuation in fluid-saturated granular rocks. Geophysics 75, N109—N120. https://doi.org/10.1190/1.3509782.
- He, Y., Wang, S., Sun, C., Tang, G., Zhu, W., 2021. Analysis of the frequency dependence characteristics of wave attenuation and velocity dispersion using a poroelastic model with mesoscopic and microscopic heterogeneities. Geophys. Prospect. 69, 1260–1281. https://doi.org/10.1111/1365-2478.13101.
- He, Y., Wang, S., Tang, G., Sun, C., Li, H., Yuan, S., Wei, X., Gan, L., Dai, X., Ge, Q., Wei, P., Zhang, H., 2024. A seismic elastic moduli module for the measurements of low-frequency wave dispersion and attenuation of fluid-saturated rocks under different pressures. Pet. Sci. 21, 162–181. https://doi.org/10.1016/j.petsci.2023.08.036.
- Huang, H., Lu, X., 2009. Relative permeabilities and coupling effects in steady-state gas-liquid flow in porous media: a lattice Boltzmann study. Phys. Fluids 21, 092104. https://doi.org/10.1063/1.3225144.
- Jakobsen, M., Chapman, M., 2009. Unified theory of global flow and squirt flow in cracked porous media. Geophysics 74, WA65–WA76. https://doi.org/10.1190/ 1.3078404.
- Jin, Z., Chapman, M., Papageorgiou, G., 2018. Frequency-dependent anisotropy in a partially saturated fractured rock. Geophys. J. Int. 215, 1985–1998. https:// doi.org/10.1093/gji/ggy399.
- Johson, D.L., 2001. Theory of frequency dependent acoustics in patchy-saturated porous media. J. Acoust. Soc. Am. 110 (2), 682–694. https://doi.org/10.1121/ 1.1381021.
- King, M.S., Marsden, R.J., 2002. Velocity dispersion between ultra-sonic and seismic frequencies in brine-saturated reservoir sandstones. Geophysics 67, 254–258. https://doi.org/10.1190/1.1451700.
- Kuteynikova, M., Tisato, N., Jänicke, R., Quintal, B., 2014. Numerical modeling and laboratory measurements of seismic attenuation in partially saturated rock. Geophysics 79, L13–L20. https://doi.org/10.1190/GEO2013-0020.1.
- Li, H., Wang, D., Gao, J., Zhang, M., Wang, Y., Zhao, L., Yang, Z., 2020. Role of saturation on elastic dispersion and attenuation of tight rocks: an experimental study. J. Geophys. Res. Solid Earth 125, e2019JB018513. https://doi.org/10.1029/2019JB018513
- Li, J., Rezaee, R., Müller, T.M., 2020. Wettability effect on wave propagation in saturated porous medium. J. Acoust. Soc. Am. 147, 911–920. https://doi.org/ 10.1121/10.0000616
- Li, J., Rezaee, R., Müller, T.M., Madadi, M., Ma, R., Sarmadivaleh, M., 2022. Wettability-dependent wave velocities and attenuation in granular porous media. Geophysics 87, MR177—MR187. https://doi.org/10.1190/geo2021-0279.1.
- Liao, J., Zhang, Q., Zhou, L., Xie, J., Xu, Y., Wang, L.X., 2023. Research on the forward-modeling method of viscoelastic Chapman extension in partially saturated rocks. Geophysics 88, MR241–MR263. https://doi.org/10.1190/ geo2022-05271.
- Luo, X., Chen, X., Liu, J., Jiang, X., Huo, F., 2022. Numerical modeling of frequency-dependent velocity and attenuation in a fractured-porous rock saturated with two immiscible fluids. J. Nat. Gas Sci. Eng. 107, 104788. https://doi.org/10.1016/j.jngse.2022.104788.

Luo, X., Chen, X., Lv, B., Liu, J., Wu, H., Wang, P., 2023. Frequency-dependent AVO inversion using a modified window-parameter-optimized S-transform for high gas-saturation reservoir delineation. Geosci. Rem. Sens. Lett. IEEE 20, 3000805. https://doi.org/10.1109/I.GRS.2023.3243846.

- Ma, R., Ba, J., Lebedev, M., Gurevich, B., Sun, Y., 2021. Effect of pore fluid on ultrasonic S-wave attenuation in partially saturated tight rocks. Int. J. Rock Mech. Min. Sci. 147, 104910. https://doi.org/10.1016/j.ijrmms.2021. 104910.
- Masson, Y.J., Pride, S.R., Nihei, K.T., 2006. Finite difference modeling of Biot's poroelastic equations at seismic frequencies. J. Geophys. Res. Solid Earth 111, B10305. https://doi.org/10.1029/2006/B004366.
- Mavko, G., Mukerji, T., Dvorkin, J., 2009. The Rock Physics Handbook-Tools for Seismic Analysis in Porous Media, second ed. Cambridge University Press, New York
- Mavko, G., Nur, A., 1975. Melt squirt in the asthenosphere. J. Geophys. Res. 80, 1444–1448. https://doi.org/10.1029/jb080i011p01444.
- Mochizuki, S., 1982. Attenuation in partially saturated rocks. J. Geophys. Res. 87, 8598–8604. https://doi.org/10.1029/JB087iB10p08598.
- Müller, T.M., Gurevich, B., Lebedev, M., 2010. Seismic wave attenuation and dispersion resulting from wave-induced flow in porous rocks - a review. Geophysics 75, A147—A164. https://doi.org/10.1190/1.3463417.
- Papageorgiou, G., Amalokwu, K., Chapman, M., 2016. Theoretical derivation of a Brie-like fluid mixing law. Geophys. Prospect. 64, 1048–1053. https://doi.org/ 10.1111/1365-2478.12380.
- Papageorgiou, G., Chapman, M., 2015. Multifluid squirt flow and hysteresis effects on the bulk modulus-water saturation relationship. Geophys. J. Int. 203, 814–817. https://doi.org/10.1093/gji/ggv333.
- Papageorgiou, G., Chapman, M., 2017. Wave-propagation in rocks saturated by two immiscible fluids. Geophys. J. Int. 209, 1761–1767. https://doi.org/10.1093/gji/ ggx128.
- de Paula, O.B., Pervukhina, M., Makarynska, D., Gurevich, B., 2012. Modeling squirt dispersion and attenuation in fluid-saturated rocks using pressure dependency of dry ultrasonic velocities. Geophysics 77, WA157—WA168. https://doi.org/ 10.1190/geo2011-0253.1.
- Pride, S.R., Berryman, J.G., Harris, J.M., 2004. Seismic attenuation due to wave-induced flow. J. Geophys. Res. Solid Earth 109, B01201. https://doi.org/10.1029/2003ib002639.
- Qi, Q.M., Muller, T.M., Gurevich, B., Lopes, S., Lebedev, M., Caspari, E., 2014. Quantifying the effect of capillarity on attenuation and dispersion in patchysaturated rocks. Geophysics 79, WB35–WB50. https://doi.org/10.1190/GE02013-0425.1.
- Qin, X., Li, X., Cao, Z., Liu, Y., 2018. The effect of water saturation on P-wave dispersion in a fractured porous medium with two immiscible fluids. J. Geophys. Eng. 15, 2556–2565. https://doi.org/10.1088/1742-2140/aadb76.
- Quintal, B., 2012. Frequency-dependent attenuation as a potential indicator of oil saturation. J. Appl. Geophys. 82, 119–128. https://doi.org/10.1016/ j.jappgeo.2012.03.001.
- Quintal, B., Caspari, E., Holliger, K., Steeb, H., 2019. Numerically quantifying energy loss caused by squirt flow. Geophys. Prospect. 67, 2196–2212. https://doi.org/10.1111/1365-2478.12832.

- Rathore, J.S., Fjaer, E., Holt, R.M., Renlie, L., 1995. P- and S-wave anisotropy of a synthetic sandstone with controlled crack geometry. Geophys. Prospect. 43 (6), 711–728. https://doi.org/10.1111/j.1365-2478.1995.tb00276.x.
- Rubino, J.G., Velis, D.R., Holliger, K., 2012. Permeability effects on the seismic response of gas reservoirs. Geophys. J. Int. 189, 448–468. https://doi.org/ 10.1111/j.1365-246X.2011.05322.x.
- Santos, J.E., Douglas Jr., J., Corberó, J., Lovera, O.M., 1990. A model for wave propagation in a porous medium saturated by a two-phase fuid. J. Acoust. Soc. Am. 87 (4), 1439–1448. https://doi.org/10.1121/1.399440.
- Sun, Y., Gurevich, B., 2020. Modeling the effect of pressure on the moduli dispersion in fluid-saturated rocks. J. Geophys. Res. Solid Earth 125, e2019JB019297. https://doi.org/10.1029/2019JB019297.
- Tisato, N., Quintal, B., 2013. Measurements of seismic attenuation and transient fluid pressure in partially saturated Berea sandstone: evidence of fluid flow on the mesoscopic scale. Geophys. J. Int. 195, 342–351. https://doi.org/10.1093/gji/ggt/259
- Wang, Z., Schmitt, D.R., Wang, R., 2017. Modeling of viscoelastic properties of nonpermeable porous rocks saturated with highly viscous fluid at seismic frequencies at the core scale. J. Geophys. Res. Solid Earth 122, 6067–6086. https:// doi.org/10.1002/2017JB013979.
- White, J.E., 1975. Computed seismic speeds and attenuation in rocks with partial gas saturation. Geophysics 40, 224–232. https://doi.org/10.1190/1.1440520.
- Yiotis, A.G., Psihogios, J., Kainourgiakis, M.E., Papaioannou, A., Stubos, A.K., 2007. A lattice Boltzmann study of viscous coupling effects in immiscible two-phase flow in porous media. Colloids Surfaces A Physicochem. Eng. Asp. 300, 35–49. https://doi.org/10.1016/j.colsurfa.2006.12.045.
- Zhang, H., He, B., 2015. Propagation and attenuation of P-waves in patchy saturated porous media. Appl. Geophys. 12, 401–408. https://doi.org/10.1007/s11770-015-0497-x.
- Zhang, J., Huang, H., Wu, C., Zhang, S., Wu, G., Chen, F., 2018. Influence of patchy saturation on seismic dispersion and attenuation in fractured porous media. Geophys. J. Int. 214, 583–595. https://doi.org/10.1093/gji/ggy160.
- Zhao, B., MacMinn, C.W., Juanes, R., 2016. Wettability control on multiphase flow in patterned microfluidics. Proc. Natl. Acad. Sci. USA. 113, 10251–10256. https:// doi.org/10.1073/pnas.1603387113.
- Zhao, B., Mohanty, K.K., 2019. Effect of wettability on immiscible viscous fingering in porous media. J. Pet. Sci. Eng. 174, 738–746. https://doi.org/10.1016/ i.petrol.2018.11.072.
- Zhao, D., Liu, C., Guo, Z., 2023. Estimation of interlayer elastic dispersion attributes based on a new frequency-dependent elastic impedance inversion method. IEEE Trans. Geosci. Rem. Sens. 61, 5921411. https://doi.org/10.1109/ TGRS.2023.3329514.
- Zhao, H., Ning, Z., Kang, Q., Chen, L., Zhao, T., 2017. Relative permeability of two immiscible fluids flowing through porous media determined by lattice Boltzmann method. Int. Commun. Heat Mass Tran. 85, 53–61. https://doi.org/10.1016/j.icheatmasstransfer.2017.04.020.
- Zhao, J., Tang, G., Deng, J., Tong, X., Wang, S., 2013. Determination of rock acoustic properties at low frequency: a differential acoustical resonance spectroscopy device and its estimation technique. Geophys. Res. Lett. 40, 2975–2982. https://doi.org/10.1002/grl.50346.